### • Original Paper •

# Aerosol-Cloud-Precipitation Interactions in a Closed-cell and Non-homogenous MBL Stratocumulus Cloud\*

Xiaojian ZHENG<sup>1</sup>, Xiquan DONG<sup>1</sup>, Dale M. WARD<sup>1</sup>, Baike XI<sup>1</sup>, Peng WU<sup>2</sup>, and Yuan WANG<sup>3</sup>

<sup>1</sup>Department of Hydrology and Atmospheric Sciences, University of Arizona, Tucson 85721, AZ, USA

<sup>2</sup>Pacific Northwest National Laboratory, Richland 99354, WA, USA

<sup>3</sup>Division of Geological and Planetary Sciences, California Institute of Technology, Pasadena 91125, CA, USA

(Received 13 January 2022; revised 18 May 2022; accepted 30 June 2022)

#### ABSTRACT

A closed-cell marine stratocumulus case during the Aerosol and Cloud Experiments in the Eastern North Atlantic (ACE-ENA) aircraft field campaign is selected to examine the heterogeneities of cloud and drizzle microphysical properties and the aerosol-cloud-precipitation interactions. The spatial and vertical variabilities of cloud and drizzle microphysics are found in two different sets of flight legs: Leg-1 and Leg-2, which are parallel and perpendicular to the cloud propagation, respectively. The cloud along Leg-2 was close to adiabatic, where cloud-droplet effective radius and liquid water content linearly increase from cloud base to cloud top with less drizzle. The cloud along Leg-1 was sub-adiabatic with lower cloud-droplet number concentration and larger cloud-droplet effective, but higher drizzle droplet number concentration, larger drizzle droplet median diameter and drizzle liquid water content. The heavier drizzle frequency and intensity on Leg-1 were enhanced by the collision-coalescence processes within cloud due to strong turbulence. The sub-cloud precipitation rate on Leg-1 was significantly higher than that along Leg-2. As a result, the sub-cloud accumulation mode aerosols and CCN on Leg-1 were depleted, but the coarse model aerosols increased. This further leads to a counter-intuitive phenomenon that the CCN is less than cloud-droplet number concentration for Leg-1. The average CCN loss rates are -3.89 cm <sup>3</sup> h <sup>1</sup> and -0.77 cm <sup>3</sup> h <sup>1</sup> on Leg-1 and Leg-2, respectively. The cloud and drizzle heterogeneities inside the same stratocumulus can significantly alter the sub-cloud aerosols and CCN budget. Hence it should be treated with caution in the aircraft assessment of aerosol-cloud-precipitation interactions.

**Key words:** maritime aerosol, cloud and drizzle properties, coalescence-scavenging effect of the sub-cloud aerosol and CCN, and aerosol-cloud-precipitation interactions

Citation: Zheng, X. J., X. Q. Dong, D. M. Ward, B. K. Xi, P. Wu, and Y. Wang, 2022: Aerosol-cloud-precipitation interactions in a closed-cell and non-homogenous MBL stratocumulus cloud. *Adv. Atmos. Sci.*, https://doi.org/10.1007/s00376-022-2013-6.

### **Article Highlights:**

- Aircraft in-situ measurements are used to examine the non-homogenous cloud adiabaticities and microphysics in the MBL stratocumulus.
- Turbulence-enhanced collision-coalescence lead to spatial and vertical variabilities of cloud and drizzle microphysics in stratocumulus.
- Coalescence-scavenging effect in the stratocumulus significantly alters the sub-cloud aerosols and CCN budgets.

### 1. Introduction

Over subtropical and mid-latitude oceans, Marine Boundary Layer (MBL) stratocumulus clouds are one of the most

 This paper is a contribution to the special issue on Cloud– Aerosol–Radiation–Precipitation Interaction: Progress and Challenges

\* Corresponding author: Xiquan DONG Email: xdong@arizona.edu dominant cloud types (Dong and Minnis, 2022)<sup>a</sup>. Due to the nature of MBL stratocumulus, which are highly reflective of shortwave radiation and weakly impactive on outgoing longwave radiation, they are a substantial modulator of the Earth's radiation balance and a crucial component in climate modeling (IPCC, 2022). Based on observations, typical mid-latitude MBL stratiform clouds exist under a temperature inversion at the top of the boundary layer, and are maintained by large-scale subsidence and cloud-top longwave radiative cooling (Lilly, 1968; Albrecht et al., 1995; Wood, 2012; Redemann

### et al., 2021; Siebert et al., 2021; Wang et al., 2021a).

Within MBL stratocumulus, cloud droplets are typically formed via condensational growth from cloud base to cloud top, and then subsequently experience the collision-coalescence process to form precipitation (Martins et al., 2011; Dong et al., 2021). Thus, MBL clouds often precipitate during their lifetime, especially in the form of drizzle (Wood, 2005; Wu et al., 2015; Dong et al., 2021). Drizzle processes are also found to be impacted by the ambient MBL environments, such as wind shear and turbulence, which can result in different microphysical properties within the MBL cloud layer (Wu et al., 2017). Drizzle drops can significantly impact not only cloud evolution, but also the MBL aerosol and cloud condensation nuclei (CCN) budgets. The drizzle drops are normally formed through cloud condensational growth and the coalescence processes near cloud top. When they start to settle, they grow by collecting more cloud droplets and drizzle self-collection until they fall from the cloud base. Hence multiple smaller cloud droplets merge to form drizzle drops, and leave larger nuclei in the sub-cloud MBL after drizzle drops evaporate. Such a process is called the coalescence scavenging effect (Wood, 2006), and it results in the net depletion of the sub-cloud aerosols and CCN number concentrations. The aerosol and CCN losses due to the coalescence scavenging effect are particularly important in the marine stratocumulus because most the drizzle drops are evaporated before they reach the surface (Dong et al., 2014; Wu et al., 2015). Additionally, the subcloud aerosols (especially coarse mode aerosols, which have diameter larger than 1 m) could also be removed by the drizzle drops only if they fall down to the surface (e.g., precipitation scavenging effect).

Previous studies using in-situ measurements, groundbased observations, and model simulations have repeatedly found that sub-cloud aerosols can alter the MBL cloud microphysical and radiative properties via the aerosol first indirect effect (FIE). That is, more aerosols induce a greater number of smaller cloud droplets (higher cloud droplet number concentration,  $N_c$ , and smaller cloud effective radius,  $r_c$ ) under constrained liquid water content conditions, and thus the MBL clouds become more reflective for incoming solar radiation (Twomey, 1977; Twohy et al., 2005; Lu et al., 2007; Bellouin et al., 2020; Zheng et al., 2020; Dong and Minnis, 2022)<sup>a</sup>. In addition to FIE, the numerous smaller cloud droplets increase the cloud residence time, occupy a broader areal extent, and affect precipitation processes, which make up the cloud adjustments to aerosol perturbations (Albrecht, 1989; IPCC, 2022; Bellouin et al., 2020).

Aerosol effects on precipitation in marine stratiform and cumulus clouds over different oceanic regions have also been investigated in multiple studies. For instance, the cloud-base drizzle rates of marine stratocumulus over the eastern and southeastern Pacific have been found to be inversely proportional to  $N_c$ , and indirectly to the sub-cloud aerosols, but the susceptibilities tend to decrease along with the cloud liquid water path (LWP) and cloud thickness (Lu et al., 2009; Terai et al., 2012). However, despite these previous studies, the MBL cloud precipitation susceptibility to aerosols still remains uncertain and inconclusive, which includes the influences of various factors such as cloud morphology, heterogeneity, LWP, aerosol species, and meteorological factors (Lu et al., 2009; Sorooshian et al., 2009; Hudson et al., 2011; Gerber and Frick, 2012; Terai et al., 2012; Chen et al., 2014; Bai et al., 2018; June et al., 2016). Therefore, further studies are necessary to acquire a deeper understanding of aerosol-cloud-precipitation interactions.

The Eastern North Atlantic (ENA) is a favorable oceanic region for studies of MBL clouds. In particular, Graciosa Island in the Azores is located between the mid-latitude and subtropical climate regimes, and is influenced by both the Icelandic Low and the Azores High, resulting in unique large-scale meteorological influences and persistent MBL stratocumulus clouds (Dong et al., 2014, 2015; Wood et al., 2015). Aerosols arriving in the ENA have diverse origins, varying from clean marine air masses to air masses that are strongly influenced by continental emissions from North America or northern Europe (Logan et al., 2014; Wood et al., 2015). As a result, the ENA is a region with strong but uncertain aerosol indirect forcing (Carslaw et al., 2013). The Atmospheric Radiation Measurement (ARM) Program has established a permanent observatory site on the northern edge of Graciosa Island (ARM-ENA, 39.09°N, 28.03°W), to aid in long-term studies of aerosol-cloud interactions in remote marine regions.

Although numerous studies have been done to investigate the MBL aerosol, cloud, and drizzle properties, as well as their interactions such as FIE and cloud adjustments at the ARM ENA site (Mann et al., 2014; Dong et al., 2015; Wood et al., 2015; Wu et al., 2017; Wang et al., 2020; Zheng et al., 2022), there are few studies that examine the heterogeneous microphysical properties of clouds and drizzle, as well as their interactions with sub-cloud aerosols and CCN (Hudson and Frisbie, 1991; Wood et al., 2012). The recent aircraft field campaign, ACE-ENA (Wang et al., 2021a), provided a great opportunity for investigating these issues. In this study, one marine stratocumulus case was selected (July 18, 2017; RF0718) during the ACE-ENA IOP. During this case, a long-lasting MBL stratocumulus with periodic drizzling events was observed over the ARM-ENA site under a well-mixed MBL condition. The aircraft flight strategy was designed to collect the data from near the sea surface to the free troposphere, following an "L" shape horizontal pattern centered over the ENA site. This case provides an invaluable opportunity to investigate the aerosol-cloud-precipitation interaction for different parts of the stratocumulus. In addition to aircraft in situ measurements, ground-based ARM observations and satellite retrievals were collected

<sup>&</sup>lt;sup>a</sup> Dong, X., and P. Minnis, 2022: Stratus, Stratocumulus and Remote Sensing, Chapter 8 of Fast Physics in Large Scale Atmospheric Models: Parameterization, Evaluation, and Observations. AGU, Manuscript ID 2020-Mar-CH-1234, in press.

and collocated with aircraft in situ measurements. These integrative observations provide information about the horizontal and vertical MBL cloud morphology and evolution as well as the horizontal and vertical variations of aerosol, cloud, and drizzle microphysical properties.

This manuscript is organized as follows: aircraft and satellite results, and the processing methods used in this study are briefly described in section 2. The horizontal and vertical differences of the MBL cloud and drizzle microphysical properties between the two defined directions and the underlying mechanisms are investigated in section 3. Section 4 discusses the horizontal differences of sub-cloud aerosols and CCN, as well as the implications of cloud heterogeneity for the aerosol-cloud-precipitation interactions. A brief summary and the conclusions, as well as the importance of this study are contained in section 5.

### 2. Data and Method

### 2.1. Cloud, Drizzle and Atmospheric States

The aircraft in situ measurements used in this study are temporally collocated at the resolution of 1 Hz, which corresponds to ~100 m of sampling given the average aircraft speed of ~100 m s<sup>-1</sup>. The cloud droplet spectrum is measured by the Fast Cloud Droplet Probe (FCDP, Glienke and Mei, 2020) onboard the G-1 aircraft, which can detect droplet sizes ranging in diameter  $(D_p)$  from 1.5  $\mu$ m to 50  $\mu$ m with resolutions of 1–3 μm at a temporal resolution of 10 Hz, and further averaged to 1 Hz. The drizzle droplet spectrum is provided by the Two-Dimensional Stereo Particle Imaging Probe (2DS, Lawson et al., 2006; Glienke and Mei, 2019), which can fully record the droplets with diameters from 5 μm to 1280 μm at 1 Hz. The merged droplet spectra are calculated by combining the FCDP ( $D_p = 2-25 \mu m$ ) and 2DS  $(D_{\rm p} = 25-1280~\mu{\rm m})$  measurements, hence the merged droplet size distribution (DSD) is from 2 μm to 1280 μm. A demarcation line of  $D_p = 40 \mu m$  is used to separate cloud droplets from drizzle drops (Wood, 2005). The cloud microphysical properties (cloud-droplet number concentration,  $N_c$ ; cloud-droplet effective radius,  $r_c$ ; liquid water content, LWC<sub>c</sub>), and drizzle (drop number concentration,  $N_d$ ; mass median diameter,  $D_{\rm md}$ ; liquid water content, LWC<sub>d</sub>) can thus be calculated based on their own DSD diameter range  $(D_{\rm p}$  = 2–40  $\mu {\rm m}$  for cloud and  $D_{\rm p}$  = 40–1280  $\mu {\rm m}$  for drizzle). A threshold of  $N_c$  5 cm<sup>3</sup> is used for determining the valid cloud samples (Wood, 2005). Note that the notations used in this study follow the study of Wu et al. (2020a) where the subscript "c" denotes cloud and subscript "d" denotes drizzle.

To investigate how different DSDs from FCDP and 2DS impact the calculated cloud and drizzle microphysical properties, we compare the calculated microphysical properties from different combinations of FCDP and 2DS with those calculated from the merged DSD used in this study. Using FCDP solely for the cloud droplet DSD (= 2–40  $\mu$ m), the mean percentage differences are 1.87%, -1.95%, and

-1.36% for  $N_c$ ,  $r_c$ , and LWC<sub>c</sub>, respectively. However, if the cloud microphysical properties are calculated mostly relying on 2DS ( $D_p = 5-40 \mu m$ ) and filling the rest with the FCDP  $(D_p = 2-5 \mu m)$ , the mean percentage differences are 15.2%, -15.1%, and -37.9%, owing to the uplifted droplet number concentrations in the small tail of the 2DS size bins, and the fact that the 2DS has a much coarser resolution in the cloud part of DSD (the first two bins of 2DS). For the drizzle DSD, if the FCDP (40–50 µm) is used in conjunction with the 2DS (50–1280 µm), the mean percentage differences are 67.3%, -12.3%, and -33.5% for  $N_d$ ,  $r_d$ , and LWC<sub>d</sub>, which is due to enhanced droplet number concentrations in the large tail of FCDP size bins. Therefore, the current combination method (2–25  $\mu m$  for FCDP and 25–1280  $\mu m$  for 2DS) used in this study is most representative of the cloud and drizzle characteristics during RF0718.

The precipitation rate (PR, in mm  $d^{-1}$ ) is estimated for the drizzle DSDs from 40  $\mu$ m to 1280  $\mu$ m:

$$PR = 24 \quad 6 \quad 10^{-4} \quad \int_{40}^{1280} D_{d}^{3} N_{d}(D_{d}) U \quad (D_{d}) dD_{d} \quad (1)$$

where  $D_d$  is drizzle drop diameter (mm),  $N_d(D_d)$  is drizzle droplet number concentration at given size bin (#m<sup>-3</sup> mm<sup>-1</sup>), and U  $(D_d)$  is the terminal velocity for a given drop size (m s <sup>1</sup>), which is estimated using the full Reynolds number theory described in Pruppacher and Klett (2010) for a temperature of 283.15 K and a pressure of 900 hPa. The aircraft position and direction, and the ambient atmospheric states (such as ambient wind, temperature, potential temperature, pressure, and specific and relative humidity) are given by the Aircraft-Integrated Meteorological Measurement System (AIMMS, Beswick et al., 2008) at a temporal resolution of 20 Hz. In addition, the large-scale cloud structure over the domain surrounding ENA during RF0718 is captured by the cloud optical depth (COD) which is retrieved from the satellite observations (NASA/LARC/SD/ Meteosat-10 ASDC, 2018).

#### 2.2. Aerosol and CCN measurements

The total aerosol number concentration  $(N_a)$  is measured by the Condensation Particle Counter (CPC, model 3772), which counts aerosol concentrations over a size range from 3 nm to 3 m (Kuang and Mei, 2020). The CPC range includes most of the Aitken, accumulation, and coarse mode aerosols, but the observations are not size-resolved, whereas the Passive Cavity Aerosol Spectrometer (PCASP) is sizeresolved for the size range from 0.1 µm to 3.2 µm (Goldberger, 2020). Therefore, the number concentrations of accumulation mode aerosol ( $N_{\rm ACC}$ , 0.1  $\mu$ m-1  $\mu$ m) and coarse mode aerosol ( $N_{> 1 \mu m}$ , 1  $\mu m$ –3.2  $\mu m$ ) can be distinguished, respectively, from the PCASP measured aerosol size spectra. The cloud condensation nuclei number concentration ( $N_{\text{CCN}}$ ) is measured by the Dual-Column CCN Counter at two constant supersaturation levels of 0.15% and 0.35% (Uin and Mei, 2019). In this study, the  $N_{\rm CCN}$  at 0.35% supersaturation  $(N_{\rm CCN35})$  is used because 0.15% is below the typical supersaturation level of the marine stratocumulus over the ENA (Logan et al., 2014; Wood et al., 2015). Note that the aerosol and CCN data are quality controlled by removing the data point where the  $N_c + N_d$  greater than 5 cm  $^3$  or  $N_d$  greater than 0.01 cm  $^3$ , in order to filter out the contamination of the cloud droplets, drizzle drops, and the splashing water. The Particle-into-Liquid Sampler (PILS) is used to examine the mass concentration of the chemical components of the ambient aerosols, with a temporal resolution of ~2 min (Watson, 2016). During ACE-ENA, the PILS was sampled with cut-off size of 1 $\mu$ m, thus the submicron aerosols were collected into the purified water for the chemical analysis. In addition, the high-resolution time-of-flight aerosol mass spec-

trometer (HR-ToF-AMS) is used to examine the mass concentration of the non-refractory submicron aerosol components, with a temporal resolution of ~13 s (Zawadowicz et al., 2021).

## 3. Heterogeneity of Cloud and Drizzle Microphysics

### 3.1. Horizontal structures of stratocumulus during RF0718

The large-scale synoptic pattern during RF0718 is illustrated by the 900-hPa geopotential heights obtained from

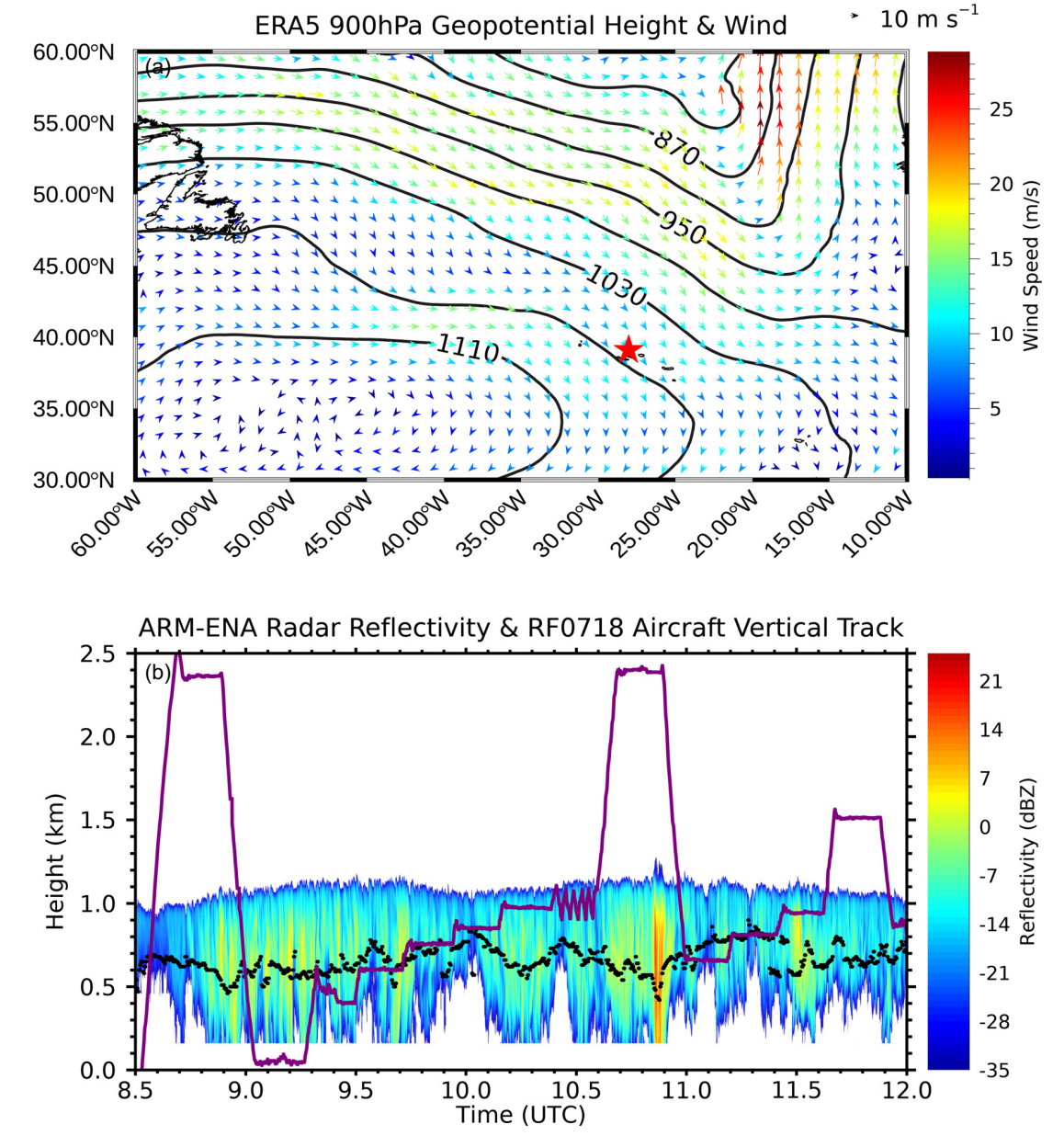


**Fig. 1.** (a) 900 hPa geopotential height (contour) and wind (arrow, color denotes wind speed) in a  $50^{\circ} \times 30^{\circ}$  domain surrounding the ENA, and the red star denotes the position of ARM-ENA site; (b) the ARM-ENA ground-based radar reflectivity (contour) overlayed by the ceilometer measured cloud base (black dot) and RF0718 aircraft vertical flight track (purple line) between 0830 to 1200 UTC.

5

ERA5 (Fig. 1a). As shown in Fig. 1a, the Azores High was located to the southwest of the ARM-ENA site, while the Icelandic Low was located on the northeastern side. Therefore, the prevailing wind during RF0718 was northwesterly. The vertical flight path is overlaid on the concurrent groundbased radar reflectivity (Fig. 1b). From ~ 0900 to 1100 UTC, the aircraft was ramping from near the sea surface up to the free troposphere. The aircraft had taken multiple horizontal flight legs accompanied by spirals when ascending or descending. Although the point-based radar reflectivity is not spatially matched with the cloud sampled by the aircraft, it provides the approximate aircraft locations, such as near the sea surface, sub-cloud, cloud-base, cloud-top and the free troposphere. This flight strategy was selected so that the aircraft sampled on one side follows the direction of the prevailing wind and the other side crosses the prevailing wind at similar height levels. Note that the flight legs collected between 1100-1200 UTC are not included in this study due to the lack of flight legs that collect sub-cloud aerosol samples and the lack of different levels of cloud samples.

To examine the horizontal structure of stratocumulus during RF0718, we plot Fig. 2 which shows the Meteosat-10 retrieved cloud optical depth (COD) over the  $2^{\circ} \times 2^{\circ}$ domain centered on the ARM ENA site at Graciosa Island. Combining the horizontal structures of COD from 900 to 1030 UTC (Fig. 2) and the Moderate Resolution Imaging Spectroradiometer (MODIS) real color image (not shown) during RF0718, we found that the study domain was dominated by a closed-cell marine stratocumulus clouds, which propagated from northwest to southeast. There were multiple bands of enhanced COD structures embedded in the stratocumulus cloud deck, and the evolution of the COD bands was generally along the direction of cloud propagation. Note that the aircraft horizontal flight path appears as an Lshaped pattern (purple lines on Fig. 2) with two directions: Leg-1 (northwest-southeast) is parallel to wind direction and cloud propagation, while Leg-2 (southwest-northeast) is perpendicular to wind direction and cloud propagation. Both legs consist of multiple flight segments at different altitudes, i.e., at each altitude or horizontal flight leg, the aircraft

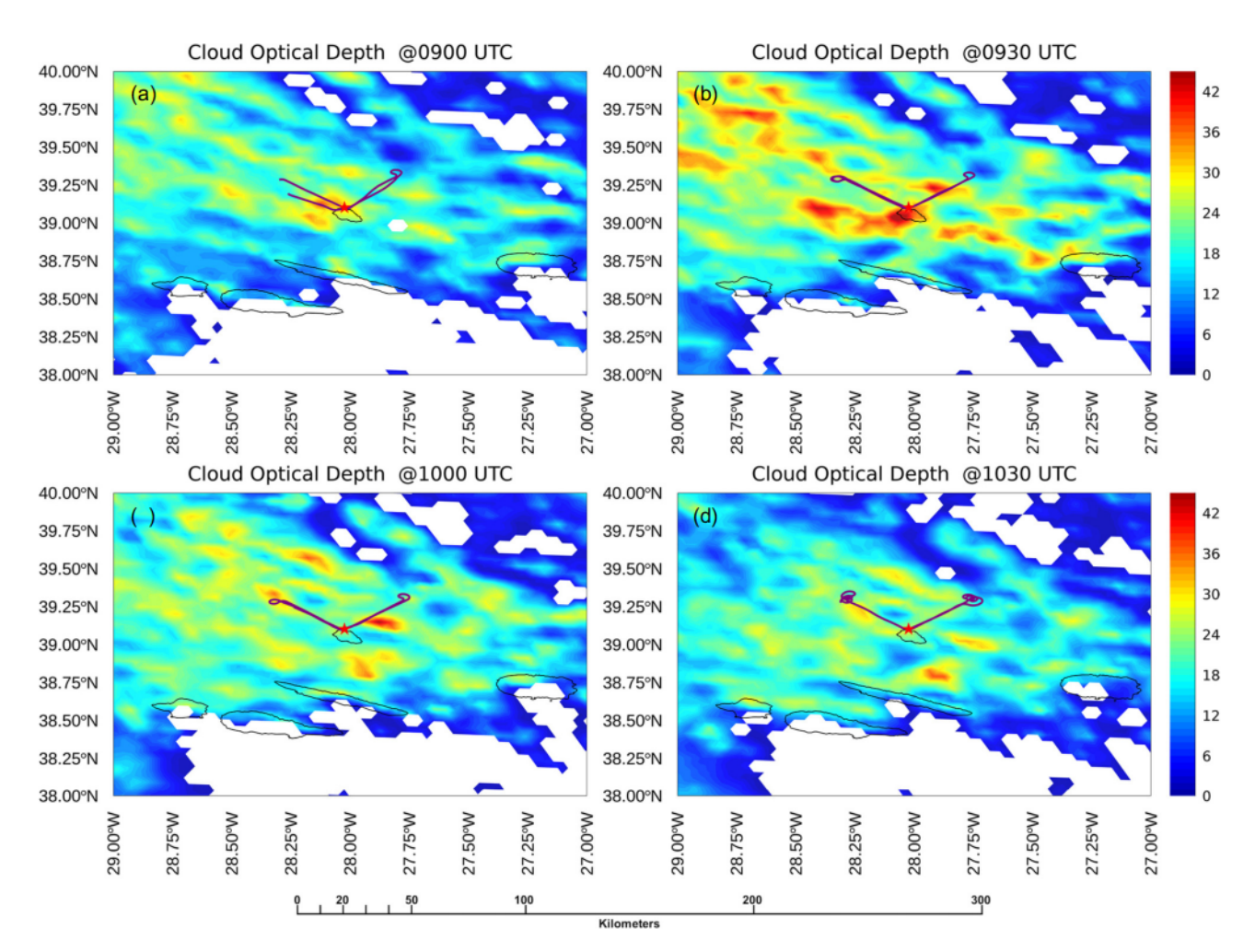


Fig. 2. Meteosat-9 measured Cloud Optical Depth over the 2° × 2° domain surrounding the RF0718 at (a) 0900 UTC; (b) 0930 UTC; (c) 1000 UTC; (d) 1030 UTC. The aircraft horizontal paths within each half hour are overlayed as purple lines with two flight directions: Leg-1 which is parallel to cloud propagation (fly from NW to SE) and Leg-2 which is perpendicular to cloud propagation (fly from SW to NE).

sampled the cloud (and/or aerosol) microphysical properties along both Leg-1 and Leg-2. These in situ measurements at each altitude are used to investigate the small-scale variation of cloud and drizzle properties in both horizontal and vertical directions. Furthermore, this flight strategy not only allows us to examine the marine stratocumulus cloud heterogeneity, but also interactions with sub-cloud aerosols, which will be discussed in the following sections.

## **3.2.** Vertical distributions of cloud and drizzle microphysical properties

Figure 3 shows the vertical distributions of cloud and drizzle microphysical properties during the aircraft legs from the sub-cloud layer to near cloud top. The samples are classified into two categories following their directions: Leg-1 and Leg-2. Note that the upper four legs (from 600 to 1000 m) in Fig. 3 represent the aircraft measurements

within the cloud layer, and the bottom legs (~400-500 m) denote the height levels below the cloud base. The  $N_c$  values for Leg-1 are consistently lower than those from Leg-2, specifically, the layer-mean  $N_c$  for Leg-1 (~64 cm<sup>-3</sup>) is about 40% less than that from Leg-2 (~ 107 cm<sup>-3</sup>). For both legs, the  $N_c$  values increased from the cloud base, maximized in the middle of the cloud, and decreased toward the cloud top (Fig. 3a). The rc and LWCc for the Leg-2 side increased almost linearly from cloud-base to cloud-top (Figs. 3b and 3c), indicating that the cloud sampled at the Leg-2 side is approximately adiabatic. On the other hand, the cloud microphysical properties along the Leg-1 side of the cloud show lower  $N_c$  and larger  $r_c$ . The layer-mean values of  $r_c$  are 11.5 µm and 10.1 µm for Leg-1 and Leg-2, respectively, with the differences in  $N_c$  and  $r_c$  having passed the 95% significance level. Furthermore, both the Nc and LWCc on the Leg-1 side show significant decreases near the cloud top.

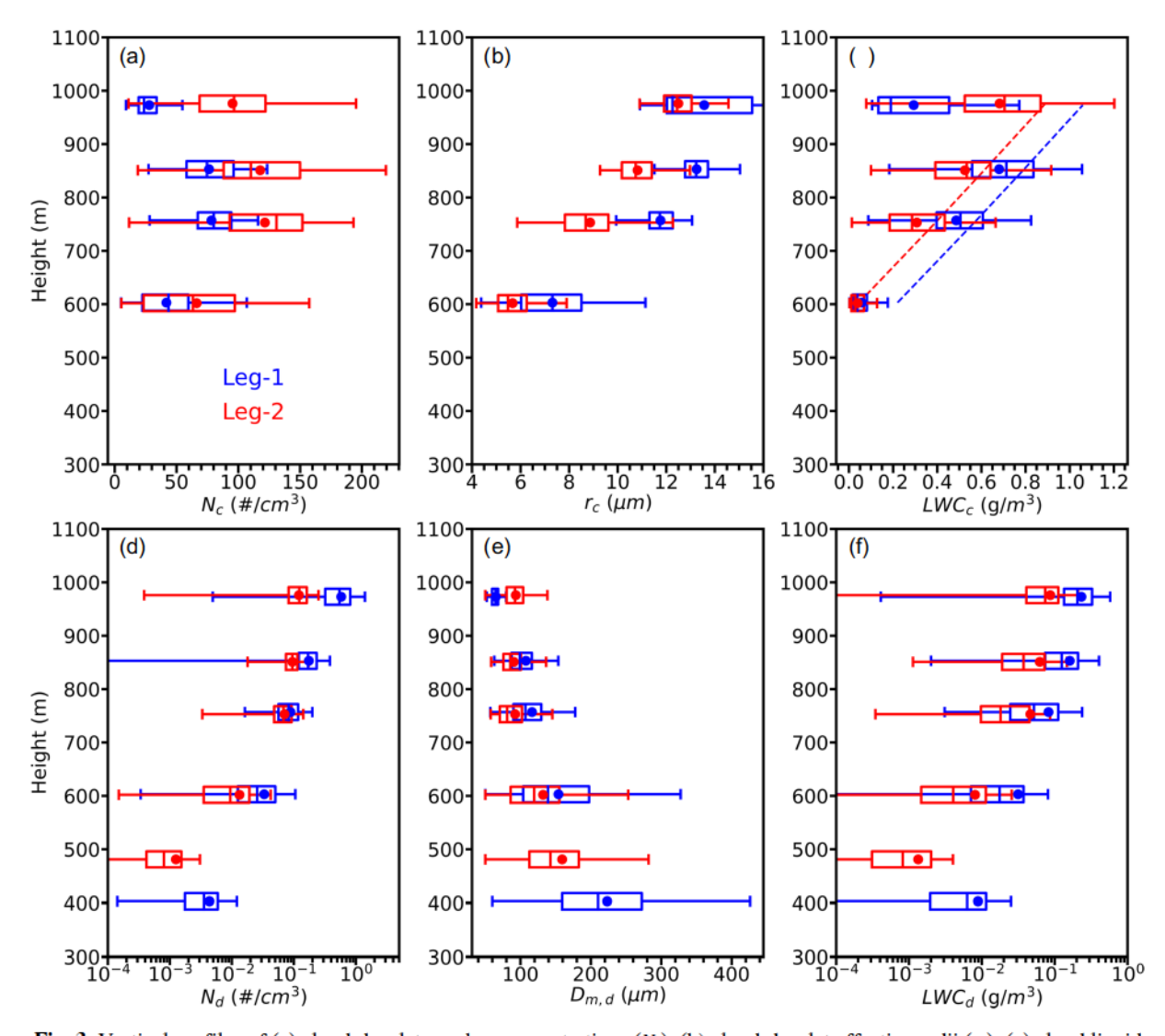


Fig. 3. Vertical profiles of (a) cloud-droplet number concentrations ( $N_c$ ); (b) cloud-droplet effective radii ( $r_c$ ); (c) cloud liquid water content (LWC<sub>c</sub>) with dashed lines denoting adiabatic LWC; (d) drizzle-drop number concentration ( $N_d$ ); (e) drizzle mass median diameter ( $D_{m,d}$ ) and (f) drizzle liquid water content (LWC<sub>d</sub>). Blue denotes sampling on Leg-1 side on L-shaped leg, and red denotes sampling on Leg-2 side on L-shaped leg. Dots show the mean values at each level, and the vertical bars from left to right represent 10%, 25%, 50%, 75%, and 90% values.

Note that the dashed lines in Fig. 3c denote the adiabatic LWC, which is calculated by LWC<sub>ad(z)</sub> =  $_{ad}(z \ z_b)$  on the two sides, where  $z_b$  is cloud base and  $_{ad}$  denotes the linear increase of LWC with height under an ideal adiabatic condition (Wood, 2005). The cloud adiabaticity ( $f_{ad}$ ) is defined as the ratio of LWC<sub>c</sub> to LWC<sub>ad</sub>. The layer mean  $f_{ad}$  is 0.56 for Leg-1 and is 0.83 for Leg-2. The difference in  $f_{ad}$  indicates that the stratocumulus cloud for Leg-1 undergoes more subadiabatic processes, while the cloud layer for Leg-2 is closer to adiabatic. These results suggest that the cloud adiabaticities are different even within the same stratocumulus cloud deck. Such characteristics of inhomogeneous mixing on a small scale were also found in previous studies on the MBL stratocumulus (e.g., Pawlowska et al., 2000; Haman et al., 2007).

Theoretically, the cloud sub-adiabaticity in the marine stratocumulus is often induced by the cloud droplet collision-coalescence and the cloud-top dry air entrainment processes (Wood, 2012; Wu et al., 2020b; Zheng et al., 2022). Notice that  $r_c$  values near the cloud top did not decrease like its  $N_c$  and LWC<sub>c</sub> counterparts because most of the small cloud droplets were either evaporated by the entrained dry air, or enlarged by the cloud droplet condensational growth and collision-coalescence, which means the cloud droplet is enlarged, but not large enough to be classified as drizzle droplet, so such large cloud droplet would contribute to  $r_c$ , but not for  $D_{\rm md}$ . This argument is supported by the distributions of  $N_c$  and LWC<sub>c</sub>, which both show longer tails toward higher values. Note that the cloud microphysical properties profiles examined in this study are similar to the results of the MBL stratocumulus clouds over the eastern South Atlantic, where  $r_c$  increases with height, and  $N_c$  and LWC<sub>c</sub> decrease with height in the upper part of cloud due to cloudtop entrainment (Diamond et al., 2018; Gupta et al., 2022).

To reveal the causality of such cloud-top reductions of  $N_c$ ,  $r_c$ , and LWC<sub>c</sub> on the Leg-1 side, we first test the hypothesis of cloud-top entrainment because it typically causes the evaporation of cloud water and results in the elimination of small cloud droplets and shrinkage of large cloud droplets. The entrainment rates for the near cloud-top legs between Leg-1 and Leg-2 are compared following the method described in Albrecht et al. (2016). The cloud-top entrainment rate ( $w_e$ ) within the stratocumulus can be estimated by:

$$w_{\rm e} = A \quad _{\rm w} R_{\rm i} \tag{2}$$

where the  $_{\rm w}$  is the standard deviation of vertical velocities near cloud top legs, and A is the coefficient associated with the dissipation of the turbulence kinetic energy budget, which was empirically estimated in the study (taken as a value of 26 in this study as per Albrecht et al., 2016). The buoyancy Richardson number  $R_{\rm i}$  at the near cloud-top leg can be calculated by:

$$R_{\rm i} = \frac{g}{{}_{0}} \quad \frac{{}_{\rm v}h}{{}_{\rm w}^{2}} \tag{3}$$

where  $_0$  is the reference potential temperature,  $_v$  is the

difference in virtual potential temperature across the MBLtop temperature inversion layer, h is the MBL depth, and  $\frac{2}{w}$ is the variance of vertical velocities. During RF0718, given the  $_{\rm w}^2$  of 0.115 m<sup>2</sup> s  $^2$ (for Leg-1) and 0.103 m<sup>2</sup> s  $^2$  (for Leg-2), the cloud-top entrainment rates are estimated to be 0.479  $\pm 0.063$  cm s <sup>1</sup> and  $0.380 \pm 0.055$  cms <sup>1</sup> for Leg-1 and Leg-2, respectively. The uncertainties of entrainment rates are estimated by propagating the uncertainties of v and h for the two sides. The difference in entrainment rates indicates the inhomogeneous mixing at the small scale, which likely is due to the small-scale variations of the thermodynamic conditions and the near-cloud-top turbulence (Haman et al., 2007; Hill et al., 2009; Lehmann et al., 2009; Gao et al., 2020). The entrainment rates fit in the general range (0.1-0.8 cm s<sup>-1</sup>) for marine stratocumulus (Nicholls and Turton, 1986; Faloona et al., 2005; Bretherton and Blossey, 2014).

The results suggest that the cloud layer on the Leg-1 side of the cloud was undergoing ~25.9% stronger dry air entrainment than that on the Leg-2 side of the cloud based on their mean values. Based on entrainment theory only, the Leg-1 side of cloud-top would have lower  $N_{\rm c}$  and LWC<sub>c</sub>. However, on average, the cloud-top Leg-1  $N_{\rm c}$  (28 cm  $^3$ ) is ~71% less than Leg-2  $N_{\rm c}$  (95 cm  $^3$ ), and Leg-1 LWC<sub>c</sub> (0.293 gm  $^3$ ) is ~57% less than Leg-2 LWC<sub>c</sub> (0.682 gm  $^3$ ). Thus, such significant differences in cloud-top microphysics cannot be solely explained by the differences in entrainment rates and are more likely also the result of the combination of the entrainment effect and the collision-coalescence processes associated with the drizzle formation and development.

The vertical profiles of drizzle drop number concentration  $(N_d)$ , mass median diameter  $(D_{md})$ , and liquid water content (LWC<sub>d</sub>) from below the cloud to the cloud-top are shown in Figs. 3d-3f. Both Leg-1 and Leg-2 sides show existing drizzle drops throughout the cloud-layer and below the cloud. From the cloud-top leg, the  $N_{\rm d}$  (0.58 cm  $^3$ ) and LWC<sub>d</sub> (0.233 gm<sup>3</sup>) on the Leg-1 side are much higher than the  $N_{\rm d}$  (0.12 cm  $^3$ ) and LWC<sub>d</sub> (0.087 gm  $^3$ ) on the Leg-2 side, whereas smaller  $D_{\rm m\,d}$  (64.9  $\mu m$ ) is observed at Leg-1 than Leg-2 (93.4  $\mu$ m). The mean ratios of  $N_d$  to  $N_c$  are 2% and 0.1%, respectively, for Leg-1 and Leg-2, suggesting that a much more effective collision-coalescence process occurred near the cloud top in the Leg-1 side of the cloud. The  $r_c$  and  $N_d$  distributions are both broader on the Leg-1 side, and their mean values are both larger than those on the Leg-2 side. These results suggest that more large cloud droplets near the cloud top experienced condensational growth and coalescence processes to form drizzle drops on the Leg-1 side, which results in more of the smaller drizzle drops (higher  $N_d$ , smaller  $D_{\rm m d}$ , more drizzle embryos) near the cloud top. Similar results were also found in other studies (e.g., Wood, 2006; Wu et al., 2020b; Dong et al., 2021). The enhanced drizzle formation process results in more drizzle embryos formed near the cloud top through the collisioncoalescence processes.

All four in-cloud aircraft legs show that the  $N_d$  and LWC<sub>d</sub> on the Leg-1 side are higher than those on the Leg-2

side. The  $D_{m\,d}$  at Leg-1 are generally larger than the Leg-2 side with broader ranges of distributions, except near the cloud top. From the cloud top to the cloud base, the mean  $N_{\rm d}$  decreased ~94% (from 0.58 to 0.033 cm<sup>-3</sup>) on the Leg-1 side, while the depletion of  $N_{\rm d}$  on the Leg-2 side is ~89% (from 0.12 to 0.013 cm<sup>3</sup>). The mean  $D_{\rm md}$  values on the Leg-1 side were consistently enlarged with a more than 137% increment at the cloud base relative to cloud top. While the  $D_{\rm md}$  on the Leg-2 side showed little variation from the cloud top to cloud center, the total increment at the cloud base is only  $\sim 41\%$ . The higher  $N_{\rm d}$  depletion rate and larger  $D_{\rm m,d}$  growth rate for Leg-1 have demonstrated a more efficient self-collection process inside the cloud layer, especially in the lower part of the cloud. When drizzle drops fall from the cloud top, they grow by collecting cloud droplets and other drizzle drops, which shows that the collision-coalescence and drizzle self-collection processes become increasingly important and result in depleted  $N_d$  and increased  $D_{\rm m\,d}$  near the cloud base. Therefore, the enhanced drizzle processes on Leg-1 side are consistent with the larger CODs retrieved from the satellite on Leg-1 side because COD is proportional to the square of  $r_c$ .

### 3.3. Mechanism of enhanced drizzle evolution

Results and discussions from the last section show that the cloud on the Leg-1 side experienced a more effective collision-coalescence process. More cloud droplets were converted to drizzle via the collision-coalescence processes, and efficiently grew to larger drizzle drops near the cloud base. The turbulence on Legs -1 and -2 were examined to further investigate a possible mechanism for the enhanced collision-coalescence characteristic. The gradient Richardson Number ( $R_i$ ) is often used to represent the thermal stability and turbulent condition of the environment (Garratt, 1994), which can be calculated from:

$$R_{i} = \frac{g}{v} - \frac{v}{z} - \frac{u^{2}}{z^{2}} + \frac{v^{2}}{z}$$
 (4)

The numerator represents the buoyancy production term of turbulence which is given by the change of virtual potential temperature across the atmospheric layer, and the denominator represents the shear production term of turbulence given by the change of horizontal wind components across the same layer. A positive  $R_i$  denotes a stable atmospheric layer while a negative  $R_i$  denotes an unstable environment. In this study, the  $R_i$  for both Leg-1 and Leg-2 were estimated using a finite difference method for each aircraft horizontal leg in the cloud layer. The variables were interpolated to ensure comparable values of z between the two sides. The  $R_i$  values, buoyancy and shear production terms of  $R_i$ , as well as the vertical velocity variances and absolute wind shears are listed in Table 1. As shown in column 8 of Table 1, for all four aircraft legs in the cloud, the  $R_i$  values on both Leg-1 and Leg-2 are negative and significantly lower than the critical value of 0.25, indicating that the MBL was unstable and turbulent.

Previous studies have shown that in-cloud turbulence can effectively enhance the drizzle production and growth processes by the turbulence-induced collision-coalescence processes (Feingold et al., 1996b; Pinsky et al., 2007). The negative  $R_i$  on both sides indicate that cloud environments were favorable to form drizzle, which is also suggested by the comparable vertical velocity variances (column 3 of Table 1) on both sides. However, the differences in the drizzle microphysics between the two sides can be better explained by breaking down the  $R_i$  into separate buoyancy (column 6 of Table 1) and shear (column 7 of Table 1) terms. The buoyancy terms are negative for all legs, indicating positive buoyancy production of turbulence (since v = z = 0), and the differences between both sides are small. The absolute values of the buoyancy term are always much larger than the shear term, which is common because buoyancy production is the primary contributor to the turbulence in MBL clouds (Nicholls, 1984; Nicholls and Leighton, 1986; Bretherton and Wyant, 1997).

However, previous studies found that the shear production also plays an important role in the turbulence generation and drizzle evolution, especially in the marine stratocumulus-topped boundary layer (Brost et al., 1982; Magaritz-Ronen et al., 2016; Wu et al., 2017). The shear terms on the Leg-1 side are noticeably larger and have higher contribution percentages (~23%–32%) in the turbulence production than the Leg-2 side (~17%–29%). Such differences in the shear

Table 1. Gradient Richardson number, Production terms, Vertical velocity variance, and Wind shears for PARL & PREP.

Leg Altitude Level	Leg Sets	Vertical Velocity Variance (m <sup>2</sup> s <sup>2</sup> )	Wind Speed Shear (ms <sup>1</sup> m <sup>1</sup> )	Wind Directional Shear (degree m 1)	Buoyancy Production (s <sup>2</sup> )	Shear Production (s <sup>2</sup> )	Gradient Richardson Number, <i>R</i> <sub>i</sub>
Near Cloud-Top	Leg-1	0.115	0.0054	0.1137	-0.528	0.259	-2.03
	Leg-2	0.103	0.0105	0.0607	-0.506	0.216	-2.34
Upper Mid-Cloud	Leg-1	0.243	0.0142	0.0901	-0.678	0.320	-2.12
	Leg-2	0.302	0.0082	0.0823	-0.665	0.188	-3.54
Lower Mid-Cloud	Leg-1	0.260	0.0095	0.0582	-0.421	0.125	-3.37
	Leg-2	0.222	0.0061	0.0514	-0.425	0.089	-4.74
Near Cloud-Base	Leg-1	0.137	0.0096	0.0971	-0.557	0.240	-2.32
	Leg-2	0.201	0.0065	0.0948	-0.543	0.178	-3.07

production terms are also supported by the generally stronger wind speed shear (column 4 of Table 1) and wind directional shear (column 5 of Table 1) on the Leg-1 side. On the one hand, the relatively stronger wind shear on the Leg-1 side, especially the upper part of the cloud, could promote drizzle formation by increasing the residence time of large cloud droplets and thus the chance of collision-coalescence among cloud droplets and/or drizzle drops (Magaritz-Ronen et al., 2016). On the other hand, strong wind shear effectively recirculates the drizzle drops in the middle and the lower part of the cloud, allowing them to grow larger by collecting smaller drizzle drops and large cloud droplets (Feingold et al., 1996b; Magaritz et al., 2009; Wu et al., 2017). Therefore, the strong wind shear enhances the efficiency of collision-coalescence processes, and results in the stronger drizzle evolution process on the Leg-1 side of the cloud. In contrast, the turbulence on the Leg-2 side is primarily driven by buoyancy, which is favorable to the updraft-dominant environment. Though buoyancy stimulates cloud-top drizzle formation, the lack of strong wind shear production limits the in-cloud efficiency of collision-coalescence and the recirculation of drizzle drops, which can explain the small variation of drizzle microphysical properties in the middle of the cloud.

## 4. Aerosol-Cloud-Precipitation Interactions during RF0718

### **4.1.** The aerosol properties below the cloud and near the surface

The aerosol FIE and cloud adjustments in marine stratocumulus, which impact the cloud microphysics, cloud lifetime, and precipitation strength, have been widely studied

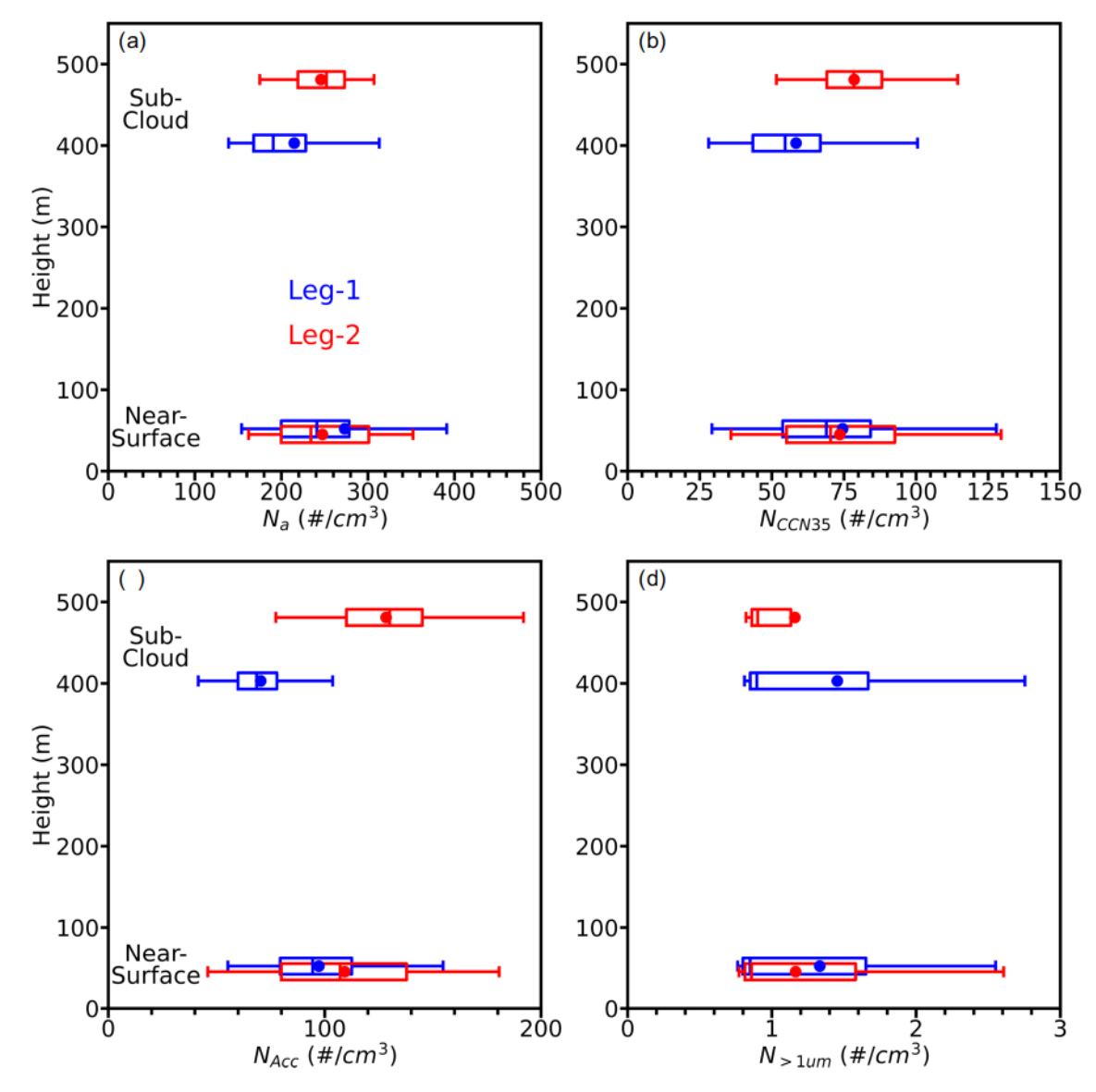


**Fig. 4.** Same as Fig. 3 except for profiles of (a) total aerosol number concentration ( $N_a$ ); (b) cloud condensation nuclei number concentration at 0.35% supersaturation ( $N_{CCN35}$ ); (c) accumulation mode aerosol number concentration ( $N_{ACC}$ ) and (d) coarse mode aerosol number concentration ( $N_{>1 \mu m}$ ).

(Twohy et al., 2005; Lu et al., 2007; Sorooshian et al., 2009; Bellouin et al., 2020). In this study, we examine whether there are differences in the aerosol-cloud-precipitation interaction induced by the cloud heterogeneity between Leg-1 and Leg-2. The observed profiles of aerosols and CCN from the sea surface to sub-cloud are shown in Fig. 4. In-cloud profiles are not shown because the aerosols and CCN counters suffered contamination from cloud water splashing during the flight. Note that the  $N_a$  (Fig. 4a) and  $N_{\text{CCN35}}$  (Fig. 4b) for both Leg-1 and Leg-2 near the sea surface are similar to each other in terms of mean values and distribution ranges. Two-sample Z-tests were performed on  $N_a$  and  $N_{CCN35}$  for two sides. The  $N_a$  and  $N_{\rm CCN35}$  have Z-statistics of 1.842 and 0.336, respectively. Considering the two-tailed Z critical value of 1.96 for a significance level of 0.05, the  $N_a$  and  $N_{\rm CCN35}$  near the sea surface are not significantly different between Leg-1 and Leg-2.

During the RF0718, the sub-cloud MBL aerosols were dominated by sulfate, with only minor contributions of nitrate and organic carbons, owing to the enhanced emission of marine dimethyl sulfate (DMS) in the summertime ENA region (Wang et al., 2020; Wang et al., 2021b). Although there were signals of long-range transport of North America continental aerosols in the free troposphere during RF0718, that continental airmass could not effectively penetrate the MBL top temperature inversion and thus could not noticeably impact the cloud microphysical properties (Wang et al., 2020). The aerosols that can potentially impact the cloud microphysical properties are primarily from the sub-cloud MBL with a rather uniform source. Near the sea surface, the accumulation mode aerosols ( $N_{ACC}$ , Fig. 4c) and coarse mode aerosols ( $N_{> 1 \mu m}$ , Fig. 4d) are significantly different between Leg-1 and Leg-2, based on the Z-test analysis. However, the mean differences between Leg-1 and Leg-2 are only 12 cm  $^3$  for  $N_{ACC}$ , and 0.17 cm  $^3$  for  $N_{>1 \text{ um}}$ , which are much smaller compared to the differences shown on the subcloud legs.

Theoretically, in the well-mixed MBL situation, such as the case of RF0718, sufficient turbulence would effectively transport the surface aerosols upward and mix through the MBL, favoring the small vertical variation of aerosols (Wang et al., 2021b; Zheng et al., 2022). However, significant differences (at 0.05 significance level) in all four variables in Fig. 4 are found for the sub-cloud legs between the two legs. Both  $N_a$  and  $N_{CCN35}$  on the Leg-1 side have lower means but with broader distributions towards higher values compared to those on the Leg-2 side. The mean  $N_{\rm ACC}$  for Leg-1 is 37.3 cm<sup>-3</sup> lower than, but its mean  $N_{> 1 \mu m}$  is 0.33 cm <sup>3</sup> higher than those on the Leg-2. Note that on the Leg-1 side, the mean  $N_{>1~\mu\mathrm{m}}$  is much greater than its median value, indicating a highly positively skewed distribution which is strongly weighted to the higher tail of  $N_{> 1 \mu m}$ . Since the major contribution of CCN comes from accumulation and coarse mode aerosols in the MBL over the ENA region (Zheng et al., 2018), we can simply estimate the mean aerosol activation rate by the percentage ratio of  $N_{\rm CCN35}$  to

the sum of  $N_{\rm ACC}+N_{\rm > 1~\mu m}$ . The activation rates from the mean values at the sub-cloud legs are 81.3% and 60.6% for Leg-1 and Leg-2, respectively. Theoretically, such discrepancy in activation rates at the same 0.35% supersaturation level would have to be due to a dramatic change in aerosol species with different activation abilities. However, previous studies (e.g., Wang et al., 2020, 2021b) and the results of RF0718 in this study do not support the hypothesis of hydrophobic aerosol intrusion (e.g., dust) in this relatively small horizontal extent of ~30 km between Leg-1 and Leg-2. Considering that the Leg-1 side has greater drizzle values, without an extra intrusion of aerosols, such discrepancies of  $N_{\rm CCN35}$ ,  $N_{\rm ACC}$  and  $N_{\rm > 1~\mu m}$  suggest interactions between aerosols and drizzle, particularly on the Leg-1 side, which warrants further consideration in the following section.

### 4.2. The Aerosol-cloud-precipitation interactions

Most aerosol FIE and cloud adjustments studies have focused on the impacts of aerosols on MBL cloud microphysical properties and lifetime, but comparatively few studies have examined the impacts of drizzle on the cloud microphysical properties near the cloud base and the sub-cloud aerosols and CCN (Wood et al., 2012; Jia et al., 2022). In this study, we investigate the impacts of drizzle on both the cloud microphysical properties near the cloud base and the sub-cloud aerosols and CCN.

The FIE accounts for the impact of the sub-cloud  $N_{\rm CCN35}$  on the cloud-base  $N_{\rm c}$  and  $r_{\rm c}$ . The FIE on  $N_{\rm c}$  and  $r_{\rm c}$ can be parameterized by the logarithmic ratio of change in  $N_{\rm c}$  or  $r_{\rm c}$  versus the change in aerosol loadings (Feingold et al., 2001, 2003; Twohy et al., 2005; McComiskey et al., 2009). At a supersaturation level of 0.35%, the  $ln(N_c)$   $ln(N_{CCN35})$  and  $ln(r_c)$   $ln(N_{CCN35})$  are calculated to be 1.56 and -0.86, respectively, from the current observations using the changes in cloud-base-leg  $N_c$  and  $r_c$ versus the change in sub-cloud-leg N<sub>CCN35</sub> between Leg-1 and Leg-2. Furthermore, even using the sum of  $N_{\rm ACC} + N_{\rm 1\ m}$  as the aerosol loading proxy (which would be less dependent on the actual supersaturation), still yields the logarithmic ratios of 0.77 and -0.42 for  $N_c$  and  $r_c$ , respectively. The results are in accord with the FIE theory in which higher CCN concentration leads to higher  $N_c$  and smaller  $r_c$ . However, the cloud microphysics susceptibilities seem out of the theoretical bounds compared with previous studies about the marine stratocumulus (Lu et al., 2007; McComiskey et al., 2009; Pandithurai et al., 2009; Zheng et al., 2022).

The results of FIEs in this study suggest that the enhanced drizzle process might amplify the calculated aerosol FIE on the Leg-1 side of the cloud. The enhanced collision-coalescence processes in the lower part of the cloud enlarged the drizzle drops and pushed both the cloud droplet and drizzle drop size distributions to larger tails as demonstrated in Figs. 3b and 3e. Thus, the same amount of increase in aerosol loadings would associate with a much greater change in  $r_{\rm c}$ , compared to the non-precipitating circumstance. As such, the existence of drizzle would yield a

much higher quantification of the cloud microphysics susceptibilities (Feingold et al., 1999; Duong et al., 2011; Jung et al., 2016; Bai et al., 2018). Furthermore, since the sub-cloud accumulation mode aerosols and CCN number concentrations were depleted by the coalescence scavenging effect, the aerosol increment would be less than the actual value before the depletion. Therefore, the magnitudes of susceptibilities are amplified since the denominators of the derivatives are smaller. Even after including the coarse mode aerosols, those susceptibilities are larger than those found in the non-precipitating MBL stratocumulus (Zheng et al., 2022).

In addition to the impacts of drizzle on the cloud droplets, the in-cloud drizzling process can also impact the sub-cloud aerosols and CCN budget via the coalescence/precipitation-scavenging effect. Under the turbulently forced incloud collision-coalescence processes, multiple smaller cloud droplets (usually formed from accumulation mode aerosols) are coalesced or collected into one large drizzle drop. When the drizzle drops fall out of the cloud base and evaporate, larger nuclei (usually in the large-accumulation or coarse mode aerosol category) remain. Furthermore, the collection of accumulation mode aerosols would be enhanced by the recirculation of drizzle in the middle and lower parts of cloud. Therefore, the coalescence scavenging effect results in the depletion and increment of the subcloud accumulation mode and coarse mode aerosols, respectively (Feingold et al., 1996a; Wood, 2006). The efficiency of the coalescence/precipitation-scavenging effect depends on MBL conditions, especially the precipitation rate (PR) below the cloud base.

The time-series of the PR,  $N_{\rm CCN35}$ ,  $N_{\rm ACC}$  and  $N_{\rm > 1~\mu m}$  of the sub-cloud legs for both Leg-1 and Leg-2 sides are plotted in Fig. 5 to examine the hypothesis of the coalescence-scavenging effect. As illustrated in Fig. 5a, more drizzle events

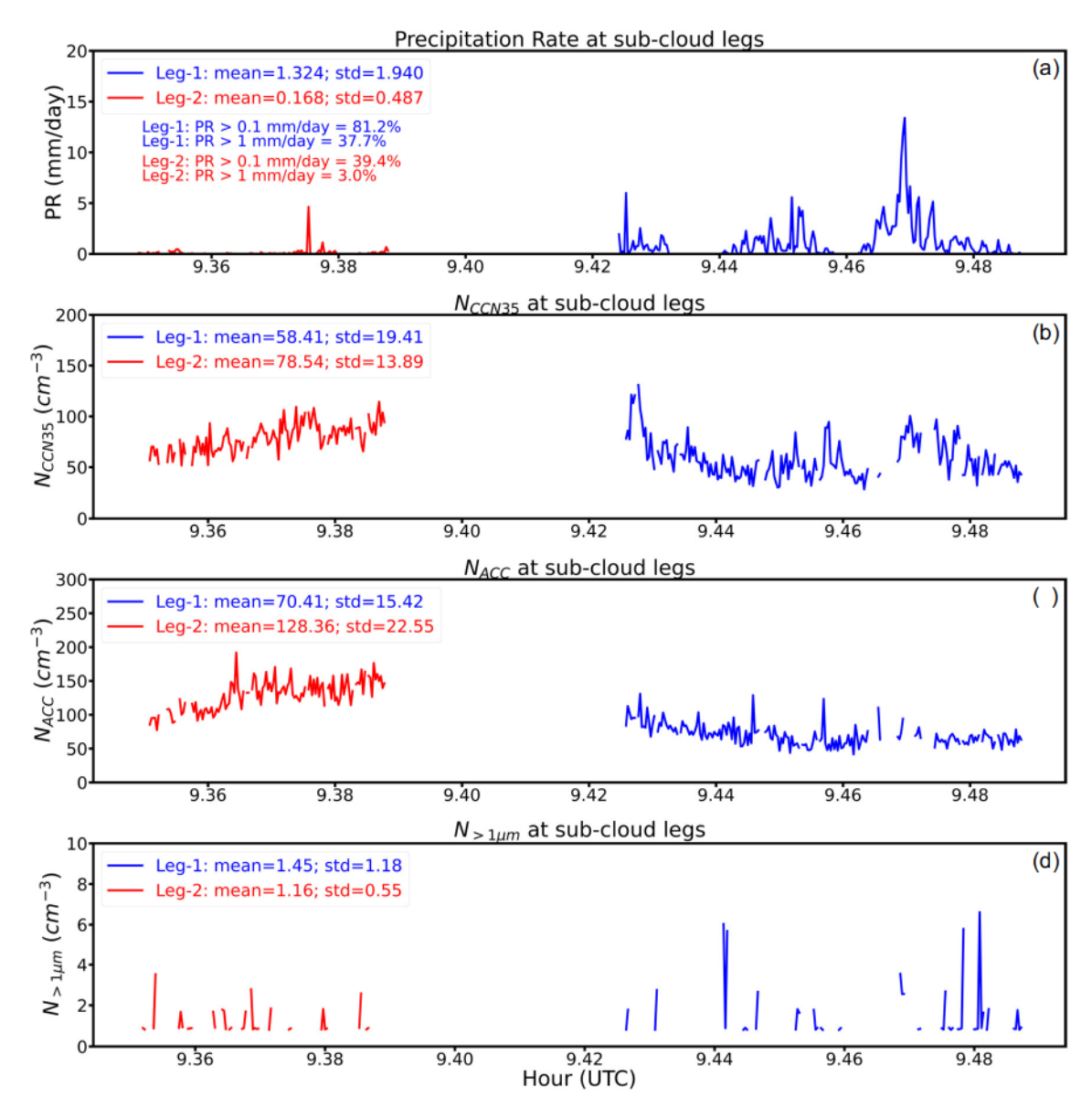


Fig. 5. Time series of (a) precipitation rate; (b)  $N_{\text{CCN35}}$ ; (c)  $N_{\text{ACC}}$  and (d)  $N_{>1 \, \mu \text{m}}$  for the sub-cloud aircraft horizontal legs.

and heavier PRs happened on the Leg-1 side. Both the  $N_{\text{CCN35}}$  (Fig. 5b) and  $N_{\text{ACC}}$  (Fig. 5c) for Leg-1, on average, are lower than those for Leg-2, whereas  $N_{> 1 \mu m}$  is opposite. Note that the empty space between the two sides denotes the turning point of the L-shaped flight path, which was right over the ARM-ENA ground site and likely suffered from the intrusion of island aerosols, hence caused the increases in both  $N_{\rm CCN35}$  and  $N_{\rm ACC}$ . It is noteworthy that on Leg-1 side, the decreases in  $N_{\rm CCN35}$  and  $N_{\rm ACC}$ , and the increase of  $N_{> 1 \mu m}$  are always lagging the PR peaks. Since at this time the aircraft was flying opposite the direction of cloud propagation, the sampled aerosols and CCN might have already experienced the coalescence scavenging. These results suggest that the coalescence/precipitation-scavenging effect is likely responsible for the observed differences in sub-cloud aerosols and CCN on both the Leg-1 and Leg-2 sides.

Moreover, the averaged aerosol size distributions for both Leg-1 and Leg-2 are compared to each other. Figure 6 clearly indicates three categories: 1) the accumulation mode aerosols (particularly in a range of 0.1–0.5 μm) are noticeably lower on the Leg-1 side, 2) they are nearly identical between 0.5-1.0 µm, and 3) the Leg-1 side has a lifted distribution in the coarse mode aerosol regime (1.0–3.2  $\mu m$ ). The results in Figs. 5 and 6 have demonstrated that the coalescence scavenging effect depletes the small-accumulation mode aerosols and lifts the remaining large-accumulation and coarse mode aerosols for the Leg-1 side. Assuming all aerosol particles are spherical, the total volumes for accumulation mode and coarse mode on the Leg-1 are 6.401 µm<sup>3</sup> and 33.90  $\mu$ m<sup>3</sup>, respectively. In addition, they are 8.862  $\mu$ m<sup>3</sup> and 13.29 μm<sup>3</sup>, respectively, for Leg-2. Thus, the volume differences between Leg-1 and Leg-2 are equivalent to one

aerosol at size of 1.01  $\mu$ m, and one coarse mode aerosol at size of 2.06  $\mu$ m. Under ideal circumstances without sulfate mass production, it would take ~8 particles with an aerosol size of 1.01  $\mu$ m to form one particle of 2.06  $\mu$ m. Since the sulfate production rate in marine stratocumulus is positively correlated with the LWC<sub>c</sub> (Pandis et al., 1994; Seinfeld and Pandis, 2016; Zheng et al., 2018), the higher in-cloud LWC<sub>c</sub> on the Leg-1 side might be favorable to produce extra sulfate mass.

To provide the chemical components of the submicron aerosols for Leg-1 and Leg-2, we plot Fig. 7 using the data collected by PILS. The Leg-1 side has both higher mass concentrations (543.86 ng m<sup>3</sup>) and percentage (50.11%) of sulfate, compared to 334.59 ng m<sup>3</sup> and 32.63% of sulfate for Leg-2. Note that the sea salt aerosols (mainly composed of sodium chloride) are much lower on the Leg-1 than on the Leg-2, indicating less remanence. The lower magnesium and sodium mass concentrations during Leg-1 may prove that more sea salt aerosols can be easily scavenged by precipitation, and the leftover of sulfate may be mainly formed by biogenic sources such as the oxidation of DMS. Additionally, the independent measurements from HR-ToF-AMS are collocated in time to provide extra evidence. The mass concentrations of non-refractory sulfates are also higher for Leg-1 (511.9 ng m<sup>-3</sup>) compared to Leg-2 (252.0 ng m<sup>-3</sup>), while the non-refractory chloride mass concentrations are much smaller for Leg-1 (12.3 ng m $^3$ ) and Leg-2 (9.5 ng m $^3$ ). Since the sea-salt aerosols are refractory and would not be detected by the HR-ToF-AMS, such results further suggest that the non-sea-salt sulfate is more dominant on the Leg-1 side, and the sea-salt aerosols are dominant on the Leg-2 side. These results support the hypothesis of a higher coalescence-scavenging effect on the Leg-1 side, as discussed

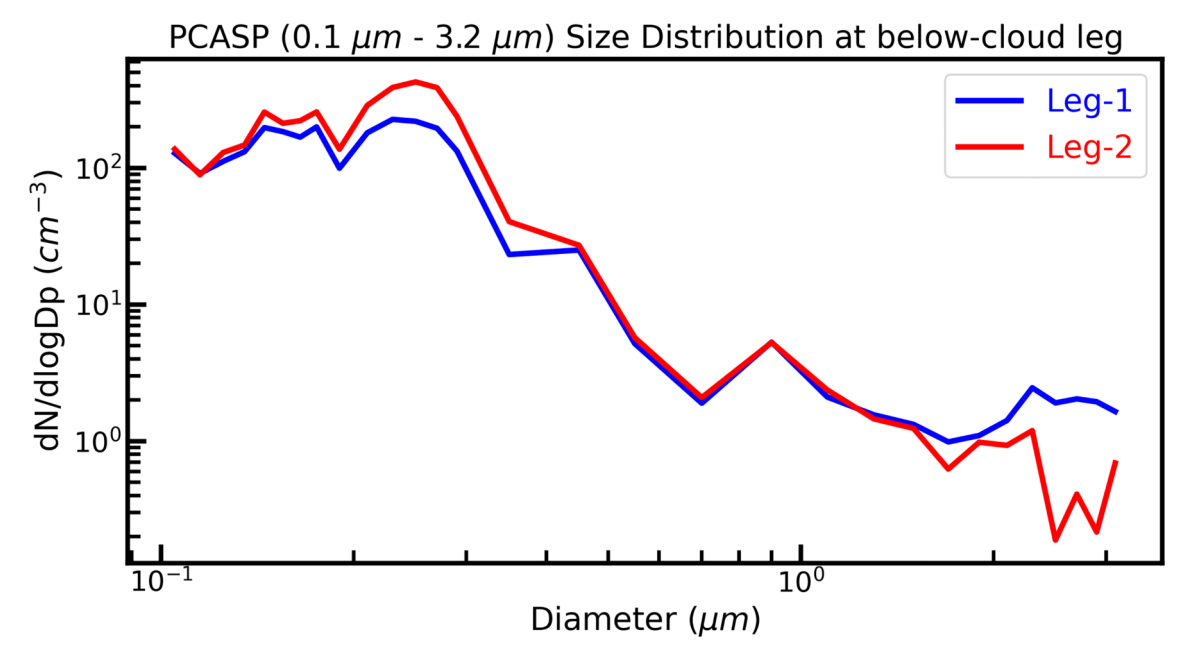
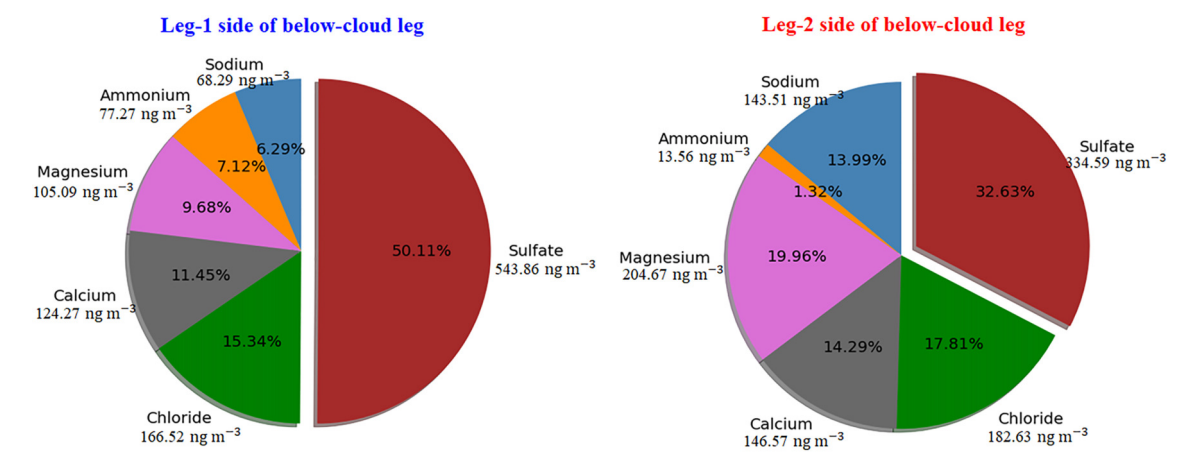


Fig. 6. Log-normal aerosol size distributions from 0.1 μm to 3.2 μm for the sub-cloud aircraft horizontal legs.



**Fig. 7.** Chart plot of mass concentrations and relative percentages of PILS sampled submicron aerosol chemical components, on Leg-1 side of sub-cloud leg (left), and on Leg-2 side of sub-cloud leg (right).

with respect to Fig. 6, because the accumulation mode aerosols in the MBL are majorly composed of sulfate. The remaining large-accumulation and coarse mode aerosols resulting from the coalescence scavenging should also be enriched with the sulfate mass.

The average loss rate of CCN ( $L_{\rm CCN}$ ) can be estimated following the method described in Wood (2005), which is given by:

$$L_{\rm CCN} = \frac{9E_0h_{\rm c}}{16_{\rm w}h}N_{\rm c} \quad PR \tag{5}$$

where  $E_0 = 4 10^3 m^{-1}$  is the fitted constant for collection efficiency,  $h_c$  is the cloud thickness, and h is the MBL depth. For the Leg-1 side of the cloud, where the layer-mean  $N_c$  is 63.79 cm  $^3$ , the sub-cloud leg  $L_{\rm CCN}$  is calculated to be  $-93.36 \text{ cm}^{-3} \text{ d}^{-1} (-3.89 \text{ cm}^{-3} \text{ h}^{-1})$ . For the Leg-2 side of the cloud, where the layer-mean  $N_c$  is 106.84 cm<sup> $\frac{3}{3}$ </sup>, and the subcloud leg  $L_{\rm CCN}$  is calculated to be -18.46 cm  $^3$  d  $^1$ (-0.77 cm  $^3$  h  $^1$ ). The estimated  $L_{\rm CCN}$  values generally fall within the ranges of the previous studies on the marine stratocumulus (Frisch et al., 1995; Bretherton et al., 2004; Wood, 2005). According to a retrospective calculation of  $N_{\text{CCN35}}$ , it would take ~6.45 hours for a uniform  $N_{\text{CCN35}}$ field of 83.51 cm<sup>3</sup> to reach the observed discrepancies between Leg-1 and Leg-2. Therefore, given the heterogeneous precipitation rates inside the same stratocumulus, the coalescence scavenging of CCN would cause systematic biases in the diagnostic CCN budget, and hence should be treated carefully in the aircraft assessment of the aerosol FIE and cloud adjustments, especially in the flight strategy that only samples parts of the cloud.

### 5. Summary and Conclusions

In this study, we use the aircraft in-situ measurements with additional satellite and ground-based radar-lidar observations to examine the heterogeneous microphysical properties of cloud and drizzle in the same stratocumulus cloud deck, as well as the implications for aerosol-cloud-precipitation

interactions. During the RF0718 of the ACE-ENA field campaign, the study domain was covered by a closed-cell marine stratocumulus propagating from northwest to southeast, with multiple enhanced COD bands embedded in the stratocumulus cloud deck. The aircraft flew in an L-shaped pattern centered on the ARM ENA site, sampling the clouds both parallel (Leg-1) and perpendicular (Leg-2) to the cloud propagation and the enhanced COD band. The results for aerosol, cloud and drizzle properties, as well as their interactions from this case study are summarized as follows.

1) The  $N_{\rm c}$  values on Leg-1 side are consistently lower than those on Leg-2 for all the in-cloud legs. The  $N_{\rm c}$  increase from the cloud base, maximize in the middle of the cloud, and decrease toward the cloud top for both sides. The  $r_{\rm c}$  and LWC<sub>c</sub> for Leg-2 linearly increase from cloud-base to the cloud-top, while they are sub-adiabatic with higher mean values on the Leg-1 side. Both the  $N_{\rm c}$  and LWC<sub>c</sub> on the Leg-1 side show significant decreases near cloud-top, indicating a more sub-adiabatic cloud environment on the Leg-1 side, which is partly contributed by the cloud-top dry air entrainment.

2) As for the drizzle properties, the  $N_{\rm d}$  and  $LWC_{\rm d}$  on all four in-cloud legs on the Leg-1 side are higher than those on the Leg-2 side. The  $D_{\rm m\,d}$  values for Leg-1 are larger than those for Leg-2 with broader size distributions. The decrease of  $N_{\rm d}$  from cloud top to cloud base for Leg-1 is greater than that for Leg-2, while the  $D_{\rm m\,d}$  values for Leg-1 consistently increase towards the cloud base. The differences in cloud and drizzle properties between Leg-1 and Leg-2 are primarily due to the turbulence-forced collision-coalescence processes. The greater buoyancy and shear production of turbulence for Leg-1 side promote an effective drizzle formation process near the cloud top and collision-coalescence and drizzle self-collection processes in the lower part of the cloud. As a result, it leads to stronger drizzle production and evolution.

3) For aerosol properties below the cloud base, both the mean values of  $N_a$  and  $N_{\rm CCN35}$  for Leg-1 are lower but with much broader distributions towards higher values compared

to those for Leg-2. The mean  $N_{\rm ACC}$  for Leg-1 is 37.3 cm  $^3$  lower than, but its mean  $N_{\rm 1~m}$  is 0.33 cm  $^3$  higher than those for Leg-2. Under the nearly same environment for both sides, the different aerosol and CCN on the two sides warrant a further study on aerosol-precipitation interactions, in particular how drizzle impacts the sub-cloud aerosols and CCN.

4) The precipitation rates on the Leg-1 side of the subcloud layer are significantly larger than those on the Leg-2 side. Therefore, the enhanced collision-coalescence processes and recirculating of drizzle drops induce a more substantial coalescence-scavenging effect on the sub-cloud aerosols and CCN, resulting in the depletion of sub-cloud accumulation mode aerosols and CCN, and an increase of coarse mode aerosol. The enhanced coalescence-scavenging effect is also evidenced by the higher mass concentration of sulfate and lower sea salt concentration in the sub-cloud aerosol on the Leg-1 side.

4) The average CCN loss rates are -3.89 cm <sup>3</sup> h <sup>1</sup> and -0.77 cm <sup>3</sup> h <sup>1</sup> for Leg-1 and Leg-2, respectively. Therefore, the heterogeneous drizzle productions and precipitation rates in the same stratocumulus can significantly alter the sub-cloud CCN budget, and it should be treated carefully in analyzing the aircraft measurements.

Future work will extend the current analysis of aerosol-cloud-precipitation interactions and the impact of MBL stratocumulus heterogeneities from a case study into more research flight cases from the ACE-ENA and other aircraft field campaigns. Furthermore, future aircraft campaigns could benefit from the flight strategy with multiple sawtooth cloud transects along the direction of cloud propagation, which would provide rather consistent representations of cloud and aerosols and shed new light on the aircraft assessment of the aerosol FIE and cloud adjustments.

This study provides observational evidence of the small-scale variability of cloud and drizzle microphysical properties inside the inhomogeneous MBL stratocumulus, which shed light on the further understanding of the usage of satellite retrievals. Since the satellite retrieved droplet number concentration heavily relies on the adiabatic cloud assumption, the misrepresentation of cloud properties, especially in the subadiabatic cloud, would induce bias in the satellite-based aerosol-cloud interaction assessment (Grosvenor et al., 2018; Quaas et al., 2020).

Furthermore, most global climate models (GCMs) underestimate marine low-level cloud fractions and overestimate MBL COD (too few but too bright problem in GCMs), which induces large variations in climate sensitivities across different GCMs (Bony and Dufresne, 2005; Zelinka et al., 2020). Due to the relatively coarse horizontal resolution of GCMs, the cloud microphysical processes cannot be fully resolved, but rather represented by simple parameterizations. The warm rain process in MBL cloud is represented by two terms, whereas the autoconversion denotes the collision-coalescence process of cloud droplets to form drizzle, and the accretion denotes the drizzle growth by collecting the cloud

droplets when they fall from cloud top to cloud base (Wu et al., 2018; Dong et al., 2021; Zhang et al., 2021). Therefore, the cloud heterogeneities, or the sub-grid variabilities of the cloud and drizzle properties within MBL stratocumulus as found in this study, should be considered by the future GCM microphysical schemes.

Acknowledgements. The aircraft in situ measurements during ACE-ENA IOP were obtained from the Atmospheric Radiation Measurement (ARM) Program sponsored by the U.S. Department of Energy (DOE) Office of Energy Research, Office of Health and Environmental Research, and Environmental Sciences Division. The data can be downloaded from https://adc.arm.gov/discovery/. This work was supported by the NSF grants AGS-2031750 and AGS-2031751, and was also supported as part of the "Enabling Aerosol-cloud interactions at GLobal convection-permitting scalES (EAGLES)" project (74358), funded by the U.S. Department of Energy, Office of Science, Office of Biological and Environmental Research, Earth System Modeling program with the subcontract to the University of Arizona. The Pacific Northwest National Laboratory is operated for the Department of Energy by Battelle Memorial Institute under Contract DE-AC05-76 RL01830. Special thanks to Dr. Timothy LOGAN at the Texas A&M University for a thorough grammar check on the manuscript. And a special thanks to the editor and three anonymous reviewers for the constructive comments and suggestions, which helped improve the manuscript.

### REFERENCES

Albrecht, B., M. Fang, and V. Ghate, 2016: Exploring stratocumulus cloud-top entrainment processes and parameterizations by using Doppler cloud radar observations. *J. Atmos. Sci.*, **73**, 729–742, https://doi.org/10.1175/JAS-D-15-0147.1.

Albrecht, B. A., 1989: Aerosols, cloud microphysics, and fractional cloudiness. *Science*, **245**, 1227–1230, https://doi.org/10.1126/science.245.4923.1227.

Albrecht, B. A., C. S. Bretherton, D. Johnson, W. H. Scubert, and A. S. Frisch, 1995: The Atlantic stratocumulus transition experiment—ASTEX. *Bull. Amer. Meteor. Soc.*, **76**, 889–904, https://doi.org/10.1175/1520-0477(1995)076 <0889:TASTE>2.0.CO;2.

Bai, H. M., C. Gong, M. H. Wang, Z. B. Zhang, and T. L'Ecuyer, 2018: Estimating precipitation susceptibility in warm marine clouds using multi-sensor aerosol and cloud products from A-Train satellites. *Atmospheric Chemistry and Physics*, **18**, 1763–1783, https://doi.org/10.5194/acp-18-1763-2018.

Bellouin, N., and Coauthors, 2020: Bounding global aerosol radiative forcing of climate change. *Rev. Geophys.*, **58**, e2019RG000660, https://doi.org/10.1029/2019RG000660.

Beswick, K. M., M. W. Gallagher, A. R. Webb, E. G. Norton, and F. Perry, 2008: Application of the Aventech AIMMS20AQ airborne probe for turbulence measurements during the Convective Storm Initiation Project. *Atmospheric Chemistry and Physics*, **8**, 5449–5463, https://doi.org/10.5194/acp-8-5449-2008.

Bony, S., and J.-L. Dufresne, 2005: Marine boundary layer clouds at the heart of tropical cloud feedback uncertainties in climate models. *Geophys. Res. Lett.*, **32**, L20806, https://doi.org/10.1029/2005GL023851.

- Bretherton, C. S., and M. C. Wyant, 1997: Moisture transport, lower-Tropospheric stability, and decoupling of cloud-topped boundary layers. *J. Atmos. Sci.*, **54**, 148–167, https://doi.org/10.1175/1520-0469(1997)054<0148:MTLTSA>2.0. CO:2.
- Bretherton, C. S., and P. N. Blossey, 2014: Low cloud reduction in a greenhouse-warmed climate: Results from Lagrangian LES of a subtropical marine cloudiness transition. *Journal of Advances in Modeling Earth Systems*, **6**, 91–114, https://doi.org/10.1002/2013MS000250.
- Bretherton, C. S., and Coauthors, 2004: The Epic 2001 Stratocumulus Study. *Bull. Amer. Meteor. Soc.*, **85**, 967–978, https://doi.org/10.1175/BAMS-85-7-967.
- Brost, R. A., J. C. Wyngaard, and D. H. Lenschow, 1982: Marine stratocumulus layers. Part II: Turbulence budgets. *J. Atmos. Sci.*, **39**, 818–836, https://doi.org/10.1175/1520-0469(1982) 039<0818:MSLPIT>2.0.CO;2.
- Carslaw, K. S., and Coauthors, 2013: Large contribution of natural aerosols to uncertainty in indirect forcing. *Nature*, 503, 67–71, https://doi.org/10.1038/nature12674.
- Chen, Y.-C., M. W. Christensen, G. L. Stephens, and J. H. Seinfeld, 2014: Satellite-based estimate of global aerosol–cloud radiative forcing by marine warm clouds. *Nature Geoscience*, 7, 643–646, https://doi.org/10.1038/ngeo2214.
- Diamond, M. S., and Coauthors, 2018: Time-dependent entrainment of smoke presents an observational challenge for assessing aerosol–cloud interactions over the southeast Atlantic Ocean. *Atmospheric Chemistry and Physics*, **18**, 14 623–14 636, https://doi.org/10.5194/acp-18-14623-2018.
- Dong, X., B. Xi, A. Kennedy, P. Minnis, and R. Wood, 2014: A 19-month record of marine aerosol-cloud-radiation properties derived from DOE ARM mobile facility deployment at the Azores. Part I: Cloud fraction and single-layered MBL cloud properties. J. Climate, 27, 3665–3682, https://doi.org/ 10.1175/JCLI-D-13-00553.1.
- Dong, X. Q., A. C. Schwantes, B. K. Xi, and P. Wu, 2015: Investigation of the marine boundary layer cloud and CCN properties under coupled and decoupled conditions over the Azores. *J. Geophys. Res. Atmos.*, **120**, 6179–6191, https://doi.org/10.1002/2014JD022939.
- Dong, X. Q., P. Wu, Y. Wang, B. K. Xi, and Y. Y. Huang, 2021: New observational constraints on warm rain processes and their climate implications. *Geophys. Res. Lett.*, **48**, e2020GL091836, https://doi.org/10.1029/2020GL091836.
- Duong, H. T., A. Sorooshian, and G. Feingold, 2011: Investigating potential biases in observed and modeled metrics of aerosolcloud-precipitation interactions. *Atmospheric Chemistry and Physics*, 11, 4027–4037, https://doi.org/10.5194/acp-11-4027-2011.
- Faloona, I., and Coauthors, 2005: Observations of entrainment in eastern Pacific marine stratocumulus using three conserved scalars. *J. Atmos. Sci.*, **62**, 3268–3285, https://doi.org/10.1175/JAS3541.1.
- Feingold, G., W. R. Cotton, B. Stevens, and A. S. Frisch, 1996a: The relationship between drop in-cloud residence time and drizzle production in numerically simulated stratocumulus clouds. *J. Atmos. Sci.*, **53**, 1108–1122, https://doi.org/10.1175/1520-0469(1996)053<1108:TRBDIC>2.0.CO;2.
- Feingold, G., S. M. Kreidenweis, B. Stevens, and W. R. Cotton, 1996b: Numerical simulations of stratocumulus processing of cloud condensation nuclei through collision-coalescence. *J. Geophys. Res. Atmos.*, 101, 21 391–21 402, https://doi.org

/10.1029/96JD01552.

- Feingold, G., A. S. Frisch, B. Stevens, and W. R. Cotton, 1999: On the relationship among cloud turbulence, droplet formation and drizzle as viewed by Doppler radar, microwave radiometer and lidar. *J. Geophys. Res. Atmos.*, **104**, 22 195–22 203, https://doi.org/10.1029/1999JD900482.
- Feingold, G., L. A. Remer, J. Ramaprasad, and Y. J. Kaufman, 2001: Analysis of smoke impact on clouds in Brazilian biomass burning regions: An extension of Twomey's approach. *J. Geophys. Res. Atmos.*, **106**, 22 907–22 922, https://doi.org/10.1029/2001JD000732.
- Feingold, G., W. L. Eberhard, D. E. Veron, and M. Previdi, 2003: First measurements of the Twomey indirect effect using ground-based remote sensors. *Geophys. Res. Lett.*, **30**, 1287, https://doi.org/10.1029/2002GL016633.
- Frisch, A. S., C. W. Fairall, and J. B. Snider, 1995: Measurement of stratus cloud and drizzle parameters in ASTEX with a  $K_{\alpha}$ -band Doppler radar and a microwave radiometer. *J. Atmos. Sci.*, **52**, 2788–2799, https://doi.org/10.1175/1520-0469 (1995)052<2788:MOSCAD>2.0.CO;2.
- Gao, S. N., C. S. Lu, Y. G. Liu, F. Mei, J. Wang, L. Zhu, and S. Q. Yan, 2020: Contrasting scale dependence of entrainment-mixing mechanisms in stratocumulus clouds. *Geophys. Res. Lett.*, 47, e2020GL086970, https://doi.org/10.1029/2020GL086970.
- Garratt, J. R., 1994: Review: The atmospheric boundary layer. *Earth-Science Reviews*, **37**, 89–134, https://doi.org/10.1016/0012-8252(94)90026-4.
- Gerber, H., and G. Frick, 2012: Drizzle rates and large sea-salt nuclei in small cumulus. *J. Geophys. Res. Atmos.*, **117**, D01205, https://doi.org/10.1029/2011JD016249.
- Glienke, S., and F. Mei, 2019: Two-dimensional stereo (2D-S) probe instrument handbook, DOE/SC-ARM-TR-233, Available from: https://www.arm.gov/publications/tech\_reports/handbooks/doe-sc-arm-tr-233.pdf.
- Glienke, S., and F. Mei, 2020: Fast cloud droplet probe (FCDP) instrument handbook, DOE/SC-ARM-TR-238, Available from: https://www.arm.gov/publications/tech\_reports/handbooks/doe-sc-arm-tr-238.pdf.
- Goldberger, L., 2020: Passive cavity aerosol spectrometer probe aboard aircraft (PCASP-AIR) with signal processing package 200 instrument handbook, DOE/SC-ARM-TR-241, Available from: https://www.arm.gov/publications/tech\_reports/handbooks/doe-sc-arm-tr-241.pdf.
- Grosvenor, D. P., and Coauthors, 2018: Remote sensing of droplet number concentration in warm clouds: A review of the current state of knowledge and perspectives. *Rev. Geophys.*, 56, 409–453, https://doi.org/10.1029/2017RG000593.
- Gupta, S., G. M. McFarquhar, J. R. O'Brien, M. R. Poellot, D. J. Delene, R. M. Miller, and J. D. S. Griswold, 2022: Factors affecting precipitation formation and precipitation susceptibility of marine stratocumulus with variable above- and below-cloud aerosol concentrations over the Southeast Atlantic. Atmospheric Chemistry and Physics, 22, 2769–2793, https://doi.org/10.5194/acp-22-2769-2022.
- Haman, K. E., S. P. Malinowski, M. J. Kurowski, H. Gerber, and J.-L. Brenguier, 2007: Small scale mixing processes at the top of a marine stratocumulus-a case study. *Quart. J. Roy. Meteor. Soc.*, 133, 213–226, https://doi.org/10.1002/qj.5.
- Hill, A. A., G. Feingold, and H. L. Jiang, 2009: The influence of entrainment and mixing assumption on aerosol–cloud interactions in marine stratocumulus. *J. Atmos. Sci.*, **66**, 1450–1464,

- https://doi.org/10.1175/2008JAS2909.1.
- Hudson, J. G., and P. R. Frisbie, 1991: Cloud condensation nuclei near marine stratus. *J. Geophys. Res. Atmos.*, **96**, 20 795–20 808, https://doi.org/10.1029/91JD02212.
- Hudson, J. G., V. Jha, and S. Noble, 2011: Drizzle correlations with giant nuclei. *Geophys. Res. Lett.*, 38, L05808, https:// doi.org/10.1029/2010GL046207.
- IPCC. Climate Change 2021: The Physical Science Basis. Contribution of Working Group I to The Sixth Assessment Report of the Intergovernmental Panel on Climate Change [Masson-Delmotte, V., et al., (eds.)]. Cambridge University Press, Cambridge, United Kingdom and New York, NY, USA, doi: 10.1017/9781009157896, in press. https://doi.org/10.5194/acp-2021-999.
- Jia, H. L., J. Quaas, E. Gryspeerdt, C. Böhm, and O. Sourdeval, 2022: Addressing the difficulties in quantifying the Twomey effect for marine warm clouds from multi-sensor satellite observations and reanalysis. Atmospheric Chemistry and Physics Discussions, 2022, 1–26,
- Jung, E., B. A. Albrecht, A. Sorooshian, P. Zuidema, and H. H. Jonsson, 2016: Precipitation susceptibility in marine stratocumulus and shallow cumulus from airborne measurements. *Atmospheric Chemistry and Physics*, 16, 11 395–11 413, https://doi.org/10.5194/acp-16-11395-2016.
- Kuang, C., and F. Mei, 2020: Condensation Particle Counter (CPC) Instrument Handbook – Airborne Version, DOE/SC-ARM-TR-227, Available from: https://www.arm.gov/publications/tech\_reports/handbooks/doe-sc-arm-tr-227.pdf.
- Lawson, R. P., D. O'Connor, P. Zmarzly, K. Weaver, B. Baker, Q. X. Mo, and H. Jonsson, 2006: The 2D-S (Stereo) probe: Design and preliminary tests of a new airborne, high-speed, high-resolution particle imaging probe. *J. Atmos. Oceanic Technol.*, 23, 1462–1477, https://doi.org/10.1175/ JTECH1927.1.
- Lehmann, K., H. Siebert, and R. A. Shaw, 2009: Homogeneous and inhomogeneous mixing in cumulus clouds: Dependence on local turbulence structure. *J. Atmos. Sci.*, **66**, 3641–3659, https://doi.org/10.1175/2009JAS3012.1.
- Lilly, D. K., 1968: Models of cloud-topped mixed layers under a strong inversion. *Quart. J. Roy. Meteor. Soc.*, **94**, 292–309, https://doi.org/10.1002/qj.49709440106.
- Logan, T., B. K. Xi, and X. Q. Dong, 2014: Aerosol properties and their influences on marine boundary layer cloud condensation nuclei at the ARM mobile facility over the Azores. *J. Geophys. Res. Atmos.*, 119, 4859–4872, https://doi.org/10.1002/ 2013JD021288.
- Lu, M.-L., W. C. Conant, H. H. Jonsson, V. Varutbangkul, R. C. Flagan, and J. H. Seinfeld, 2007: The marine stratus/stratocumulus experiment (MASE): Aerosol-cloud relationships in marine stratocumulus. *J. Geophys. Res. Atmos.*, 112, D10209, https://doi.org/10.1029/2006JD007985.
- Lu, M.-L., A. Sorooshian, H. H. Jonsson, G. Feingold, R. C. Flagan, and J. H. Seinfeld, 2009: Marine stratocumulus aerosolcloud relationships in the MASE-II experiment: Precipitation susceptibility in eastern Pacific marine stratocumulus. *J. Geophys. Res. Atmos.*, 114, D24203, https://doi.org/10.1029/2009JD012774.
- Magaritz-Ronen, L., M. Pinsky, and A. Khain, 2016: Drizzle formation in stratocumulus clouds: Effects of turbulent mixing. *Atmospheric Chemistry and Physics*, **16**, 1849–1862, https://doi.org/10.5194/acp-16-1849-2016.
- Magaritz, L., M. Pinsky, O. Krasnov, and A. Khain, 2009: Investi-

- gation of droplet size distributions and drizzle formation using a new trajectory ensemble model. Part II: Lucky parcels. *J. Atmos. Sci.*, **66**, 781–805, https://doi.org/10.1175/2008JAS2789.1.
- Mann, J. A. L., J. Christine Chiu, R. J. Hogan, E. J. O'Connor, T. S. L'Ecuyer, T. H. M. Stein, and A. Jefferson, 2014: Aerosol impacts on drizzle properties in warm clouds from ARM Mobile Facility maritime and continental deployments. *J. Geophys. Res. Atmos.*, 119, 4136–4148, https://doi.org/10.1002/2013JD021339.
- Martins, J. V., and Coauthors, 2011: Remote sensing the vertical profile of cloud droplet effective radius, thermodynamic phase, and temperature. *Atmospheric Chemistry and Physics*, **11**, 9485–9501, https://doi.org/10.5194/acp-11-9485-2011.
- McComiskey, A., and Coauthors, 2009: An assessment of aerosolcloud interactions in marine stratus clouds based on surface remote sensing. *J. Geophys. Res. Atmos.*, **114**, D09203, https: //doi.org/10.1029/2008JD011006.
- NASA/LARC/SD/ASDC. 2018: SatCORPS CERES GEO Edition 4 meteosat-10 northern hemisphere version 1.2. Available from https://cmr.earthdata.nasa.gov/search/concepts/C1588 128371-LARC\_ASDC.html.
- Nicholls, S., 1984: The dynamics of stratocumulus: Aircraft observations and comparisons with a mixed layer model. *Quart. J. Roy. Meteor. Soc.*, **110**, 783–820, https://doi.org/10.1002/qj. 49711046603.
- Nicholls, S., and J. Leighton, 1986: An observational study of the structure of stratiform cloud sheets: Part I. Structure. *Quart. J. Roy. Meteor. Soc.*, **112**, 431–460, https://doi.org/10.1002/gi.49711247209.
- Nicholls, S., and J. D. Turton, 1986: An observational study of the structure of stratiform cloud sheets: Part II. Entrainment. *Quart. J. Roy. Meteor. Soc.*, 112, 461–480, https://doi.org/ 10.1002/qj.49711247210.
- Pandis, S. N., L. M. Russell, and J. H. Seinfeld, 1994: The relationship between DMS flux and CCN concentration in remote marine regions. *J. Geophys. Res. Atmos.*, **99**, 16 945–16 957, https://doi.org/10.1029/94JD01119.
- Pandithurai, G., T. Takamura, J. Yamaguchi, K. Miyagi, T. Takano, Y. Ishizaka, S. Dipu, A. Shimizu, 2009: Aerosol effect on cloud droplet size as monitored from surface-based remote sensing over East China Sea region. *Geophys. Res. Lett.*, **36**, L13805, https://doi.org/10.1029/2009GL038451.
- Pawlowska, H., J. L. Brenguier, and F. Burnet, 2000: Microphysical properties of stratocumulus clouds. *Atmos. Res.*, 55, 15–33, https://doi.org/10.1016/S0169-8095(00)00054-5.
- Pinsky, M. B., A. P. Khain, and M. Shapiro, 2007: Collisions of cloud droplets in a turbulent flow. Part IV: Droplet hydrodynamic interaction. *J. Atmos. Sci.*, **64**, 2462–2482, https://doi.org/10.1175/JAS3952.1.
- Pruppacher, H. R., and J. D. Klett, 2010: Microphysics of Clouds and Precipitation. Springer, 954pp, https://doi.org/10.1007/978-0-306-48100-0.
- Quaas, J., and Coauthors, 2020: Constraining the Twomey effect from satellite observations: Issues and perspectives. *Atmospheric Chemistry and Physics*, **20**, 15 079–15 099, https://doi.org/10.5194/acp-20-15079-2020.
- Redemann, J., and Coauthors, 2021: An overview of the ORA-CLES (ObseRvations of Aerosols above CLouds and their intEractionS) project: Aerosol-cloud-radiation interactions in the southeast Atlantic basin. Atmospheric Chemistry and Physics, 21, 1507–1563, https://doi.org/10.5194/acp-21-

1507-2021.

- Seinfeld, J. H., and S. N. Pandis, 2016: *Atmospheric Chemistry and Physics: From Air Pollution to Climate Change*. 3rd ed. John Wiley & Sons, 1152pp.
- Siebert, H., and Coauthors, 2021: Observations of aerosol, cloud, turbulence, and radiation properties at the top of the marine boundary layer over the Eastern North Atlantic Ocean: The ACORES campaign. *Bull. Amer. Meteor. Soc.*, **102**, E123–E147, https://doi.org/10.1175/BAMS-D-19-0191.1.
- Sorooshian, A., G. Feingold, M. D. Lebsock, H. L. Jiang, and G. L. Stephens, 2009: On the precipitation susceptibility of clouds to aerosol perturbations. *Geophys. Res. Lett.*, 36, L13803, https://doi.org/10.1029/2009GL038993.
- Terai, C. R., R. Wood, D. C. Leon, and P. Zuidema, 2012: Does precipitation susceptibility vary with increasing cloud thickness in marine stratocumulus. *Atmospheric Chemistry and Physics*, 12, 4567–4583, https://doi.org/10.5194/acp-12-4567-2012.
- Twohy, C. H., and M. D. Petters, J. R. Snider, B. Stevens, W. Tahnk, M. Wetzel, L. Russell, F. Burnet, 2005: Evaluation of the aerosol indirect effect in marine stratocumulus clouds: Droplet number, size, liquid water path, and radiative impact. *J. Geophys. Res. Atmos.*, 110, D08203, https://doi.org/10.1029/2004JD005116.
- Twomey, S., 1977: The Influence of Pollution on the Shortwave Albedo of Clouds. *J. Atmos. Sci.*, **34**, 1149–1152, https://doi.org/10.1175/1520-0469(1977)034<1149:TIOPOT>2.0.
- Uin, J., and F. Mei, 2019: Cloud condensation nuclei particle counter instrument handbook airborne version, DOE/SC-ARM-TR-225, Available from: https://www.arm.gov/publications/tech\_reports/handbooks/doe-sc-arm-tr-225.pdf.
- Wang, J., and Coauthors, 2021a: Aerosol and cloud experiments in the Eastern North Atlantic (ACE-ENA). *Bull. Amer. Meteor. Soc.*, **103**, E619–E641, https://doi.org/10.1175/BAMS-D-19-0220.1.
- Wang, Y., X. J. Zheng, X. Q. Dong, B. K. Xi, P. Wu, T. Logan, and Y. L. Yung, 2020: Impacts of long-range transport of aerosols on marine-boundary-layer clouds in the eastern North Atlantic. *Atmospheric Chemistry and Physics*, 20, 14 741–14 755, https://doi.org/10.5194/acp-20-14741-2020.
- Wang, Y., and Coauthors, 2021b: Vertical profiles of trace gas and aerosol properties over the eastern North Atlantic: Variations with season and synoptic condition. *Atmospheric Chemistry and Physics*, 21, 11 079–11 098, https://doi.org/10. 5194/acp-21-11079-2021.
- Watson, T. B., 2016: Particle-into-liquid sampler instrument handbook, DOE/SC-ARM-TR-162, Available from: https://www. arm.gov/publications/tech\_reports/handbooks/pils\_handbook.pdf.
- Wood, R., 2005: Drizzle in Stratiform boundary layer clouds. Part I: Vertical and horizontal structure. *J. Atmos. Sci.*, **62**, 3011–3033, https://doi.org/10.1175/JAS3529.1.
- Wood, R., 2006: Rate of loss of cloud droplets by coalescence in warm clouds. *J. Geophys. Res. Atmos.*, **111**, D21205, https://doi.org/10.1029/2006JD007553.
- Wood, R., 2012: Stratocumulus clouds. Mon. Wea. Rev., 140, 2373–2423, https://doi.org/10.1175/MWR-D-11-00121.1.
- Wood, R., D. Leon, M. Lebsock, J. Snider, and A. D. Clarke, 2012: Precipitation driving of droplet concentration variability in marine low clouds. *J. Geophys. Res. Atmos.*, **117**, D19210, https://doi.org/10.1029/2012JD018305.

Wood, R., and Coauthors, 2015: Clouds, aerosols, and precipitation in the marine boundary layer: An arm mobile facility deployment. *Bull. Amer. Meteor. Soc.*, **96**, 419–440, https://doi.org/10.1175/BAMS-D-13-00180.1.

- Wu, P., X. Dong, and B. Xi, 2015: Marine boundary layer drizzle properties and their impact on cloud property retrieval. *Atmospheric Measurement Techniques*, 8, 3555–3562, https://doi. org/10.5194/amt-8-3555-2015.
- Wu, P., X. Q. Dong, B. K. Xi, Y. G. Liu, M. Thieman, and P. Minnis, 2017: Effects of environment forcing on marine boundary layer cloud-drizzle processes. *J. Geophys. Res. Atmos.*, 122, 4463–4478, https://doi.org/10.1002/2016JD026326.
- Wu, P., B. K. Xi, X. Q. Dong, and Z. B. Zhang, 2018: Evaluation of autoconversion and accretion enhancement factors in general circulation model warm-rain parameterizations using ground-based measurements over the Azores. *Atmos. Chem. Phys.*, 18, 17 405–17 420, https://doi.org/Atmospheric Chemistry and Physics.
- Wu, P., X. Q. Dong, B. K. Xi, J. J. Tian, and D. M. Ward, 2020a: Profiles of MBL cloud and drizzle microphysical properties retrieved from ground-based observations and validated by aircraft in situ measurements Over the Azores. *J. Geophys. Res. Atmos.*, 125, e2019JD032205, https://doi.org/10.1029/ 2019JD032205.
- Wu, P., X. Q. Dong, and B. K. Xi, 2020b: A climatology of marine boundary layer cloud and drizzle properties derived from ground-based observations over the Azores. *J. Climate*, 33, 10 133–10 148, https://doi.org/10.1175/JCLI-D-20-0272.
- Zawadowicz, M. A., and Coauthors, 2021: Aircraft measurements of aerosol and trace gas chemistry in the eastern North Atlantic. *Atmospheric Chemistry and Physics*, **21**, 7983–8002, https://doi.org/10.5194/acp-21-7983-2021.
- Zelinka, M. D., T. A. Myers, D. T. McCoy, S. Po-Chedley, P. M. Caldwell, P. Ceppi, S. A. Klein, K. E. Taylor, 2020: Causes of higher climate sensitivity in CMIP6 models. *Geophys. Res. Lett.*, 47, e2019GL085782, https://doi.org/10.1029/2019GL085782.
- Zhang, Z., and Coauthors, 2021: Vertical dependence of horizontal variation of cloud microphysics: Observations from the ACE-ENA field campaign and implications for warm-rain simulation in climate models. *Atmospheric Chemistry and Physics*, 21, 3103–3121, https://doi.org/10.5194/acp-21-3103-2021.
- Zheng, G., and Coauthors, 2018: Marine boundary layer aerosol in the eastern North Atlantic: Seasonal variations and key controlling processes. *Atmospheric Chemistry and Physics*, **18**, 17 615–17 635, https://doi.org/10.5194/acp-18-17615-2018.
- Zheng, X. J., B. K. Xi, X. Q. Dong, T. Logan, Y. Wang, and P. Wu, 2020: Investigation of aerosol–cloud interactions under different absorptive aerosol regimes using Atmospheric Radiation Measurement (ARM) southern Great Plains (SGP) ground-based measurements. Atmospheric Chemistry and Physics, 20, 3483–3501, https://doi.org/10.5194/acp-20-3483-2020.
- Zheng, X. J., B. K. Xi, X. Q. Dong, P. Wu, T. Logan, and Y. Wang, 2022: Environmental effects on aerosol-cloud interaction in non-precipitating marine boundary layer (MBL) clouds over the eastern North Atlantic. *Atmospheric Chemistry and Physics*, 22, 335–354, https://doi.org/10.5194/acp-22-335-2022.